Breakup of nocturnal low-level stratiform clouds during the southern West African Monsoon Season

Maurin ZOUZOUA[1], Fabienne LOHOU[2], Paul ASSAMOI[1], Marie LOTHON[2], Véronique YOBOUE[1], Cheikh DIONE[3], Norbert KALTHOFF[4], Bianca ADLER[4], Karmen BABIĆ[4], and Xabier PEDRUZO-BAGAZGOITIA[5]

[1]Laboratoire de Physique de l'atmosphère et de Mécanique des fluides (LAPA-MF), Université Félix Houphouët Boigny, Abidjan, Côte d'Ivoire
[2]Laboratoire d'Aérologie, Université de Toulouse, CNRS, UPS, Toulouse, France
[3]African Centre of Meteorological Applications for Development, Niamey, Niger
[4]Institute of Meteorology and Climate Research, Karlsruhe Institute of Technology (KIT), Karlsruhe, Germany
[5]Meterology and Air Quality Group, Wageningen University and Research, Wageningen, the Netherlands

Correspondence to: Maurin ZOUZOUA (maurin.zouzoua@aero.obs-mip.fr)

Abstract.

Within the framework of DACCIWA (Dynamics-Aerosol-Chemistry-Cloud-Interactions over West Africa) project, and based on a field experiment conducted in June and July 2016, we analyze the daytime breakup of the continental low-level stratiform clouds in southern West Africa. We use the observational data gathered during twenty-two precipitation-free occurrences at Savè, in Benin. Our analysis, which starts from the stratiform cloud formation usually at night, focuses on the role played by the coupling between the cloud and the surface in the transition towards shallow convective clouds during daytime. It is based on several diagnostics, including Richardson number and various cloud macrophysical properties. The distance between lifting condensation level and cloud base height is used as a criterion of coupling. We also make an attempt to estimate the most predominant terms of the liquid water path budget on early morning.

When the nocturnal low-level stratiform cloud forms, it is decoupled from the surface, except in one case. On early morning, the cloud is found coupled with the surface in nine cases and remains decoupled in the thirteen other cases. The coupling, which occurs within the four hours after the cloud formation, is accompanied with a cloud base lowering and near-neutral thermal stability in the subcloud layer. Further, at the initial stage of the transition, the stratiform cloud base is slightly cooler, wetter and more homogeneous in the coupled cases. The moisture jump at cloud top is found usually around 2 g kg^{-1}, and the temperature jump within 1-5 K, which is significantly smaller than typical marine stratocumulus, and explained by the monsoon flow environment within which the stratiform cloud develops. No significant difference of liquid water path budget terms was found between the coupled and decoupled cases. In agreement with previous numerical studies, we found that the stratiform cloud maintenance before the sunrise results from the interplay between the predominant radiative cooling, and the entrainment and large scale subsidence at its top.

Three transition scenarios were observed, depending on the state of the coupling at the initial stage. In the coupled cases, the low-level stratiform cloud remains coupled until its breakup. In five of the decoupled cases, the cloud couples with the

surface as the LCL is rising**. In the eight remaining cases, the stratiform cloud remains hypothetically decoupled from the surface all along its life cycle, since the cloud base height remains separated from the condensation level**. In case of coupling during the transition, the stratiform cloud base lifts with the growing convective boundary layer roughly between 06:30 and 08:00 UTC. The cloud deck breakup occurring at 11:00 UTC or later leads to the formation of shallow convective clouds. When the decoupling subsists, shallow cumulus clouds form below the stratiform cloud deck between 06:30 and 09:00 UTC. The breakup time in this scenario has a stronger variability, and occurs before 11:00 UTC in most of the cases. Thus we argue that the coupling with the surface during the daytime hours has a crucial role in the low-level stratiform cloud maintenance and in its transition towards shallow convective clouds.

Keywords: Stratiform cloud breakup, surface coupling, liquid water path budget, DACCIWA experiment.

1 Introduction

The low-level stratiform clouds (LLSC) are Earth's most common cloud type (Wood, 2012). During the West Africa monsoon season, the LLSC form frequently at night over a region extending from Guinean coast to several hundred kilometres inland (van der Linden et al., 2015), which includes the coastal, Sudanian and Sudanian-Sahelian climatic zones (Emetere, 2016). The LLSC coverage persists for many hours during the following day, reducing the incoming solar radiation, and impacting the surface energy budget and related processes such as the diurnal cycle of the atmospheric boundary layer (ABL) (Schuster et al., 2013; Adler et al., 2017; Knippertz et al., 2017). However, the diurnal cycle of those clouds is still poorly represented in numerical weather and climate models, especially over West Africa (Hannak et al., 2017). Indeed, their lifetime is generally underestimated in the numerical simulations, causing high incoming solar radiation at the surface in this region where the meteorological conditions are governed by convection activities and by surface thermal and moisture gradients (Knippertz et al., 2011). This could be an important factor for which the forecasts of West African monsoon features still have a poor skill (Hannak et al., 2017). Therefore, a better understanding of the processes behind LLSC over southern West Africa (SWA) is useful to improve the numerical weather prediction and climate projection quality. Due to the scarce weather monitoring network over West Africa, the first studies addressing the LLSC over this region were mostly conducted with satellite images and traditional synoptic observations (Schrage and Fink, 2012; van der Linden et al., 2015), as well as with numerical simulations at regional scale (Schuster et al., 2013; Adler et al., 2017; Deetz et al., 2018). They emphasized that the physical processes, spanning from local to synoptic scale such as horizontal advection of cold air associated to West African monsoon, lifting induced by topography, gravity waves or shear-driven turbulence, are relevant for the LLSC formation during the night. However, the LLSC evolution after the sunrise received little attention.

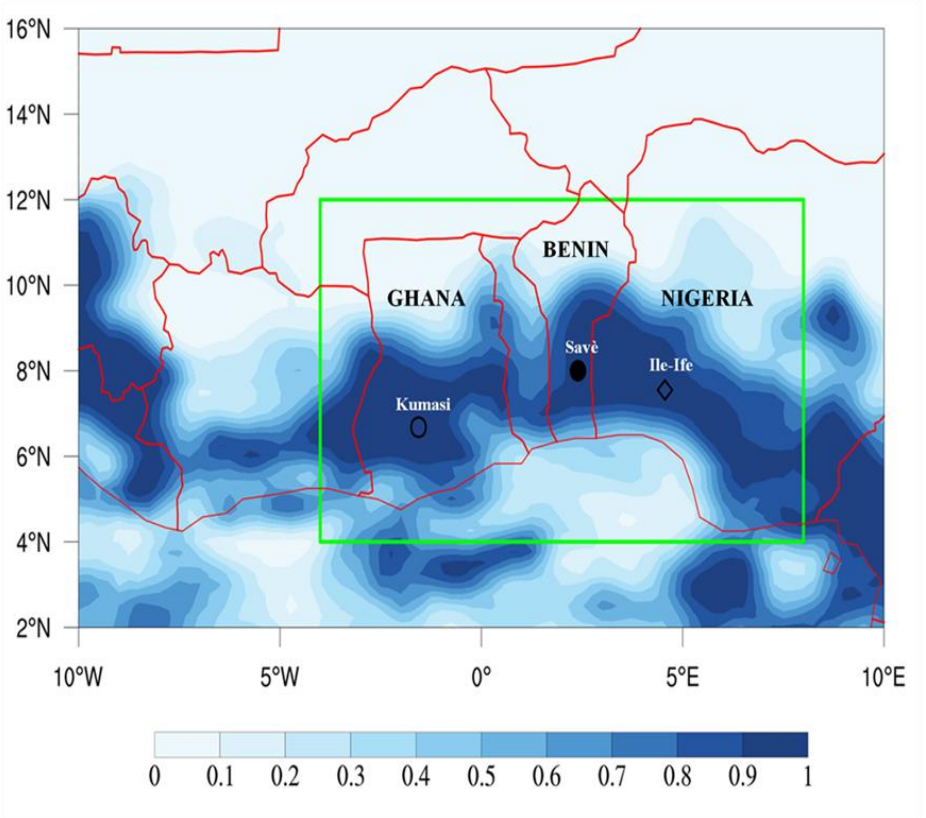

Figure 1. Low-level cloud fraction over West Africa from ECMWF (European Centre for Medium range Weather Forecast) ERA5 re-analyses (Copernicus Climate Change Service, 2019), averaged between 05:00 and 07:00 UTC on 8 July 2016. The fraction varies from 0 (clear sky) to 1 (totally covered sky). The red lines represent the geopolitical boundaries. The green box delimits the area of interest during DACCIWA field campaign. The black markers indicate the geographical locations of DACCIWA ground supersites Savè in Benin (filled circle), Kumasi in Ghana (unfilled circle) and Ile-Ife in Nigeria (unfilled diamond).

During the boreal summer 2016, a field campaign was conducted over SWA within the framework of the European project Dynamics-Aerosol-Chemistry-Cloud Interaction in West Africa (DACCIWA) (Knippertz et al., 2015). The project was developed to study the impact of increasing air pollution on SWA weather and climate. A joint measurement, including aircraft and ground-based campaigns (Flamant et al., 2017; Kalthoff et al., 2018), was performed. The area of interest during this field experiment is indicated in Fig. 1, which gives an overview of the LLSC horizontal extent between 05:00 and 07:00 UTC on 8 July 2016. One of the primary goals of this project was to provide the first high quality and comprehensive dataset in order to conduct a detailed observational study of the LLSC. **To this end, three so-called "supersites", which gather a large set of complementary instruments, were installed at Kumasi (6.68° N, 1.56° E) in Ghana, Savè (8.00° N, 2.40° W) in Benin, and Ile-Ife (7.55° N, 4.56° W) in Nigeria (Fig. 1).** The comprehensive dataset acquired at the Savè supersite allowed the first research studies of LLSC over SWA based on high temporal resolution observations. Adler et al. (2019) and

Babić et al. (2019a,b) studied the physical processes which govern the LLSC formation and its maintenance up to the next day. Dione et al. (2019) performed a statistical analysis on the LLSC characteristics and low troposphere dynamic features during the DACCIWA field campaign. The findings of these studies have been generalized and synthesized by Lohou et al. (2020) who also quantified for the first time the impact of the LLSC on the surface energy budget terms. These observational-based studies focused mainly on the mechanisms involved in the formation of LLSC during the West Africa monsoon season, to evaluate the hypotheses proposed by earlier research works. They confirmed the role played by the horizontal advection and vertical wind shear driven by a nocturnal low-level jet (NLLJ) which is among the main features of the West African monsoon (Parker et al., 2005; Lothon et al., 2008). The breakup of the LLSC deck after the sunrise which leads to the transition towards shallow convective clouds has not been well documented yet with the unique DACCIWA dataset. Only Pedruzo-Bagazgoitia et al. (2019) analyzed this transition by the mean of idealized Large Eddy Simulations (LES), inspired by the data collected during the LLSC occurrence on 25-26 June 2016 at the Savè supersite. This was the first LES of stratocumulus to shallow cumulus (Sc-Cu) transition over land in SWA.

Our study aims at analyzing the transition from the LLSC to shallow convective clouds of twenty-two cases observed at Savè supersite during DACCIWA experiment, addressing the possible scenarios and the involved processes, as far as enabled by the available measurements. This should provide a complementary guidance for numerical model evaluation of this Sc-Cu transition over SWA. The rest of this paper is organized as follow. Section 2 presents a brief state of our knowledge on the diurnal cycle of, the LLSC covering the SWA, and stratocumulus at other places around the world with a focus on the Sc-Cu transition. Section 3 describes the observational data and the deduced diagnostics used to monitor the LLSC evolution. It also overviews how the contributions of some processes involved in the LLSC diurnal cycle are derived from the measurements. Section 4 presents the LLSC characteristics just before the sunrise, at the initial stage of the transition. The relative contributions of the physical processes governing the LLSC are estimated. In section 5, the evolution of LLSC on daylight hours is analyzed. Finally, a summary and conclusion are given in section 6.

2 Review

The diurnal cycle of the LLSC over SWA consists of four main stages: the *stable phase*, the *jet phase*, the *stratus phase* and the *convective phase* (Babić et al., 2019a; Lohou et al., 2020). **The increase of relative humidity (Rh) within the ABL leading to saturation and LLSC formation is due to the cooling which mainly occurs during the stable and the jet phases in the monsoon layer, up to around 1.5 km above ground level (a.g.l.).** The main process behind this cooling is the horizontal advection of cooler air from Guinea coast, due to the combination of a maritime inflow (MI) (Adler et al., 2017; Deetz et al., 2018) and the NLLJ (Schrage and Fink, 2012; Dione et al., 2019). The onset time and the strength of the NLLJ, as well as the level of background humidity in the ABL, are crucial for the LLSC formation (Babić et al., 2019b). Indeed, from two case studies, Babić et al. (2019b) showed that weaker and later NLLJ onset leads to a reduced cooling, so

that the saturation within the ABL may not be reached. The formation of the LLSC marks the end of the jet phase and the beginning of the *stratus phase*. The LLSC base is firstly located around the NLLJ core where the cooling is maximum (Adler et al., 2019; Babić et al., 2019a; Dione et al., 2019; Lohou et al., 2020). During the *stratus phase*, the maximum wind speed in the NLLJ is reduced and shifted upward by the turbulent mixing induced by the longwave radiative cooling at the cloud-top, typical characteristic of stratocumulus clouds. In addition, the dynamical turbulence underneath the NLLJ and the convective turbulence due to the cloud top cooling are potential drivers of the coupling between the LLSC and the surface (Adler et al., 2019; Lohou et al., 2020). This dynamical turbulence could also be an important factor for additional cooling below the LLSC base (Babić et al., 2019a). When the LLSC is coupled to the surface, its base coincides quite well with the surface-based lifting condensation level (LCL) (Adler et al., 2019; Lohou et al., 2020). The final *convective phase* of the LLSC diurnal cycle starts after sunrise, when the sensible heat flux becomes larger than 10 W m^{-2}, and ends at the cloud layer breakup (Dione et al., 2019; Lohou et al., 2020).

A comprehensive overview on the current state of research on the stratocumulus dynamic is presented by Garratt (1994) and Wood (2012). Such a cloud is regulated through feedbacks between several processes: radiation, precipitation, turbulence fluxes of moisture and heat at cloud base, entrainment and large-scale subsidence at the cloud top. The cloud Liquid Water Path (LWP) budget is considered to disentangle the respective contribution of each process. **During night-time, the longwave radiative cooling at the stratocumulus top is the leading process governing its maintenance. This cooling occurs because the cloud droplets emit more infrared radiation towards the free troposphere than they receive from the drier air above. It is modulated by cloud-top temperature, cloud optical thickness, thermodynamic and cloudy conditions in the free-troposphere (Siems et al., 1993; Wood, 2012; Christensen et al., 2013; Zheng et al., 2019).** After the sunrise, the solar radiation comes into play, warming the cloud, and penetrating more and more down to the surface as the cloud layer breaking occurs. The LES performed by Ghonima et al. (2016) revealed that the effect of turbulent fluxes at cloud base depends upon Bowen ratio (B) at the surface, where B is the ratio of surface sensible flux to latent flux. Low values of B contribute to cloud layer humidification, favouring cloud persistence. In contrast, the predominance of surface sensible heat over latent heat flux ($B > 1$) warms the cloud, leading to its evaporation. The precipitation formation, the large-scale subsidence and entrainment have generally drying and warming effects on the cloud layer (Wood, 2012; van der Dussen et al., 2016).

The Sc-Cu transition in other climatologic regions was the subject of several studies, most of them made over the ocean (e.g. Bretherton et al., 1999; Duynkerke et al., 2004; Sandu and Stevens, 2011; van der Dussen et al., 2016; de Roode et al., 2016; Mohrmann et al., 2019; Sarkar et al., 2019), and a few over land (e.g. Price, 1999; Ghonima et al., 2016). In these studies, the stratocumulus is initially coupled to the surface with the convective turbulence produced by the cloud-top radiative cooling. The processes-analyzed studies, essentially based on numerical simulations, proposed specific mechanisms for the cloud layer breakup, but still based on an enhancement of entrainment warming and drying effect. Over land especially, the main driver is the intensification of the convection within the ABL by the solar heating.

The LES made by Pedruzo-Bagazgoitia et al. (2020) provide an insight on the evolution of a coupled LLSC to surface in terms of involved processes in the SWA monsoon conditions. Before the sunrise, the cloud-top radiative cooling is the unique positive contribution to the LWP budget and is the factor which maintains the cloud layer. The breakup of the cloud deck five hours after the sunrise is mainly due to the progressive decrease of cloud-top cooling, and to the increase of cloud-top entrainment negative contribution to LWP budget. About thirty minutes before the stratiform cloud deck breakup, a negative buoyancy flux at its base decouples it from the surface. Later on, a shallow cumulus cloud fully coupled to the surface appears at the top of the convective ABL. **Since the LES made by Pedruzo-Bagazgoitia et al. (2020) are set with atmospheric and surface conditions measured at Savè during the DACCIWA campaign, some simplifying assumptions used in our study are based on their results, and the simulated and observational results are compared**.

3 Data and Methodology

The period in which the DACCIWA field experiment took place (June-July 2016) was divided in four synoptic phases by Knippertz et al. (2017), based on the north-south precipitation difference between the coastal and Sudanian-Sahelian areas. The first phase, the pre-onset phase, ends on 16 June 2016 with a northward shift of the rainfall, indicating the settlement of the West Africa monsoon season (Fitzpatrick et al., 2015). The second synoptic phase, the post-onset phase, characterized by higher rainfall over the Sudanian-Sahelian zone, lasted from 22 June to 20 July 2016. During the first days of this phase, namely from 27 June to 8 July 2016, undisturbed monsoon flow and an increase of low-level cloudiness were observed over SWA, especially over DACCIWA investigated area. Between 9 and 16 July 2016, the formation of the nocturnal LLSC over SWA was inhibited by drier conditions in the low troposphere due to an unusual anticyclonic vortex which had its center in the Southern Hemisphere (Knippertz et al., 2017; Babić et al., 2019b). During the third phase, from 21 to 26 July 2016, the rainfall maximum shifts back to the coastal zone and a strong westerly flow was observed in the low-troposphere over the Sudanian-Sahelian zone. At last, during the final synoptic phase named the recovery phase, meteorological conditions return to a more typical behaviour for the monsoon season, with a precipitation maximum in the Sahel and low-troposphere dynamic similar to the beginning of the post-onset phase.

The DACCIWA supersites were located at roughly the same distance from the Guinean coast (200 km in land, Fig. 1), between the coastal and the Sudanian areas, but with a different topography (Kalthoff et al., 2018). The supersites are part of the savannah ecosystem, where grassland is intercut with crops and degraded forest. By using the ground-based data, Kalthoff et al. (2018) give an overview of the low-troposphere diurnal cycle at these three ground sites. The DACCIWA field campaign includes fifteen intensive observation periods (IOPs) during which the temporal resolution of the radiosondes performed at the supersites, especially at Savè, was improved. Each IOP lasted from 17:00 UTC on one given day (day-D) to 11:00 UTC on the following day (day-D+1).

The ground-based data acquired at Savè supersite on which our investigation is based offer nearly continuous information on atmospheric conditions. The instrumentation and the data collected correspond to four published DOI (Derrien et al., 2016; Handwerker et al., 2016; Kohler et al., 2016; Wieser et al., 2016). We analyzed a set of twenty-two LLSC occurrences for which the cloud forms during night and persists at least until sunrise the next day. These cases have been selected over the period from 20 June to 31 July 2016, because of good data coverage (Dione et al., 2019). Only cases for which the stratus phase, determined by the methodology of Adler et al. (2019), started before 04:00 UTC on day-D+1 have been selected. Additionally, for each selected cases, no or light precipitation, i.e. less than 1 mm, was recorded at the surface from 21:00 UTC on day-D to 16:00 UTC on day-D+1. Among these twenty-two cases, nine are IOPs, including the 07-08 July 2016 (IOP8) case (Babić et al., 2019a) and the 25-26 June 2016 case (IOP3) (Pedruzo-Bagazgoitia et al., 2020). About 60% of the selected cases occurred between the 26 June and 11 July 2016, a period which roughly fits within the first three weeks of the post-onset phase, and is characterized by a low-troposphere dynamic typical for West Africa monsoon season. **Note that we hereafter consider UTC time rather than Benin local time (UTC + 1 hour).**

3.1 Instrumentation

Two complementary and co-located instruments installed at Savè supersite were used to provide information on the LLSC macrophysical characteristics: a ceilometer for the cloud base height (CBH), and a cloud radar for the cloud top height (CTH).

Through backscatter vertical profiles measured by the ceilometer, from the surface to 15 km a.g.l with a vertical resolution of 15 m, manufacturer software automatically provides each minute three estimates of CBH allowing the detection of several cloudy layers. As we focus on the LLSC (the lowest cloudy layer), we use only the lowest value (hereafter CBHs). The LLSC top height (CTHs) are derived from 5-min averaged radar reflectivity vertical profiles from 150 m to 15 km a.g.l at a vertical resolution of 30 m, by a methodology described in Babić et al. (2019) and Adler et al. (2019). According to Dione et al. (2019), the LLSC top evolves overall under 1200 m a.g.l. To be consistent with this outcome, an upper limit of 1200 m a.g.l was applied to the CTHs. U**nfortunately, several values of CTHs are missing, particularly during daytime for many selected cases, due to the retrieval technique limitation.**

The thermodynamical and dynamical characteristics of the low troposphere are retrieved from the radiosondes of the MODEM radiosounding system. The MODEM radiosonde collects every second (which corresponds to a vertical resolution of 4-5 m) the air temperature and relative humidity, and the probe GPS localization from which horizontal wind speed components, altitude and pressure are deduced (Derrien et al., 2016). The sensors accuracy is 0.2 °C, 2 % and 0.01 m for temperature, relative humidity and GPS localization respectively. A standard radiosonde was launched every day at 05:00 UTC and usually rose up to 14 km a.g.l. On IOP days, three additional radiosondes were performed at 23:00 UTC on day-D, and at 11:00 and 17:00 UTC on day-D+1. In between these soundings, so-called re-usable radiosondes were more frequently launched at regular time interval in order to provide higher temporal resolution of the conditions

within the ABL. The re-usable radiosondes reached a maximum height of around 1500 m a.g.l. During the first six IOPs of DACCIWA, the frequent soundings were performed hourly and each 1.5 h during the other IOPs. The radiosondes data were averaged at a final vertical resolution of 50 m. Additionally, measurements of an ultra-high frequency (UHF) wind profiler are used to derive the NLLJ core height at 15 min time interval (Dione et al., 2019).

The meteorological conditions at the surface (temperature, relative humidity and pressure of the air at 2 m a.g.l), and some terms of the surface energy budget (net radiative flux (R_{n0}) sensible heat (SHF_0) and latent heat (LHF_0) fluxes at 4 m a.g.l) were continuously acquired. SHF_0 and LHF_0 are deduced from high-frequency (20 Hz) measurements processed with Eddy-covariance methods by using the TK3.11 software (Mauder et al., 2013).

3.2 Derived diagnostics to monitor the LLSC

We define some diagnostics to monitor the evolution of the LLSC layer: the *fraction of the low cloud coverage*, the *LLSC base height* and *the homogeneity of the cloud layer*, the *link between the LLSC and the surface*, as well as two *characteristic times of the LLSC evolution*. The LLSC depth would also be a key diagnostic, but the low availability of CTHs cloud radar-based estimates during daytime limits the cloud depth monitoring. In addition to that, the humidity and temperature sensors onboard the radiosonde were affected by the water deposition during the crossing of the LLSC layer, so neither these are fully reliable for the CTH estimate (Adler et al., 2019; Babić et al., 2019a).

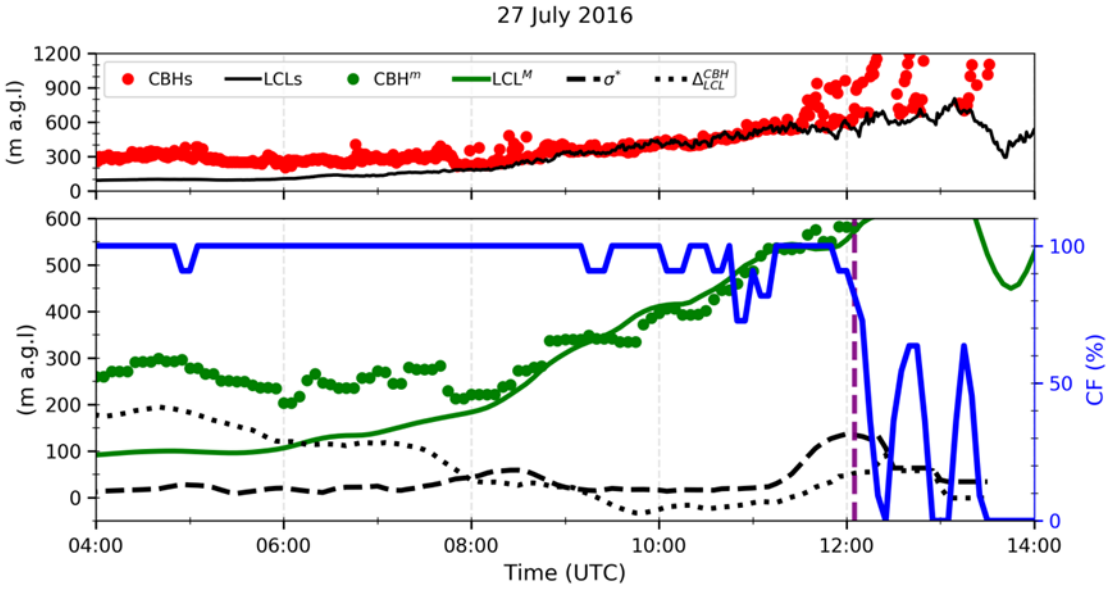

Figure 2 : Time series of, 1-min ceilometer-derived CBHs and surface-based lifting condensation level (LCLs) (upper panel), and derived 5-min diagnostics (lower panel), minimum of CBHs (CBH^m), mean LCLs (LCL^M, full green line), standard deviation of the difference between CBHs and CBH^m (σ*, dashed black line), the difference between CBH^m et LCL^M (Δ_{LCL}^{CBH}, dotted black line) and cloud coverage fraction (CF, full blue line), between 04:00 and 14:00 UTC on 27 July 2016. The vertical dashed purple line marks the breakup time of the LLSC layer (T_b). The Local time at Savè (in Benin) is UTC +1 hour.

The diagnostics are calculated over a time interval of 10 minutes with a moving window of 5 minutes, which roughly corresponds to the convective time scale. Figure 2 illustrates our methodology, with an example of the measurements and the derived diagnostics for the case of 26-27 July 2016.

- *Fraction of the low cloud coverage*: The low-cloud fraction (*CF*) is defined as the percentage of 1-min ceilometer CBHs lower than or equal to 1000 m a.g.l. Thus, *CF* greater or equal to 90% corresponds to the presence of LLSC. A similar methodology was used by Adler et al. (2019), but with a threshold of 600 m a.g.l. We extend the upper limit to 1000 m a.g.l to take into account of the rising of the LLSC base during the *convective phase* (Lohou et al., 2020). On 27 July 2016 (Fig. 2), the few periods between 04:00 UTC and 11:30 UTC with CF < 90% indicate intermittent break within the LLSC deck. This feature is common to many other cases.

- *LLSC base height and homogeneity of the cloud layer:* As seen in Fig. 2, the cloud "base height" may be more or less homogeneous in time and space, from a compact level cloud deck (like from 06:00 UTC to 06:30 UTC in Fig. 2) to a fragmented cloud layer or even separated cumulus clouds (like from 12:30 UTC to 13:00 UTC in Fig. 2). In the latter case, the ceilometer beam often hits cumulus cloud base or higher edges introducing a large variability of the so-called and measured "CBH" (which is here more rigorously the first height above ground, with detected clouds). In order to take this aspect into account in the definition of the LLSC base, and to quantify the LLSC base homogeneity, we define two other diagnostics based on the 1-min ceilometer-derived CBHs. The first one is a characteristic LLSC base height, defined as the minimum of CBHs over the 10-min intervals (CBH^m). The second, is the standard deviation of CBHs (<=1000 m a.g.l) minus CBH^m within the 10-min intervals (σ^*), which gives an insight on the LLSC layer heterogeneity by deleting the effect of CBH morning increase (Lohou et al., 2020). Small values of σ^* indicate nearly constant CBHs, that is horizontally homogenous base of the cloud layer (like from 04:00 UTC to 07:00 UTC on 27 July). High values of σ^* indicate irregular bases of the LLSC layer or a mix of cloud base and edges after the LLSC breakup (like around 12:00 UTC on 27 July). The increase of σ^* from 21 to 135 m after 11:00 UTC on 27 July (Fig. 2), typically indicates an evolution towards a more heterogeneous LLSC layer.

- *Link between the LLSC and the surface:* When a stratiform cloud is coupled to the surface, its base coincides rather well with the LCL (Zhu et al., 2001; Wood, 2012). So that, the coupling between the LLSC and the surface may be assessed by the distance between the cloud base height and the LCL. We define LCL^M as the mean value of LCL calculated on 10-min time interval by the use of Romps (2017) formulation with near surface meteorological measurements. The coupling is estimated by $\Delta_{LCL}^{CBH} = CBH^m - LCL^M$. On 27 July 2016 (Fig. 2), Δ_{LCL}^{CBH} is initially around 190 m, from 04:00 to 06:00 UTC, indicating that the LLSC is decoupled from the surface. The progressive increase of the LCL starting around 06:00 UTC leads to the LLSC coupling with the surface slightly before 08:00 UTC.

Finally, the diagnostics LCL^M, Δ_{LCL}^{CBH} and σ^* defined before are smoothed with a moving average over 30 minutes every 5 min (Fig. 2).

- *Characteristic times of the LLSC evolution:* From the above diagnostics, two specific times characterizing the LLSC lifetime are determined.

• The surface-convection influence time (T_i) corresponding to the time from which the low-level cloud coverage reacts to solar heating at the surface. The method to determine T_i depends on the evolution of LLSC during the *convective phase*. Thus, it will be precisely defined later in the text, after the presentation of the different observed scenarios.

• The LLSC breakup time (T_b) which corresponds to the end of the LLSC occurrence. It is the time (after 06:30 UTC) from which *CF* is lower than 90% during at least one hour. Figure 2 (lower panel) shows several periods, between 09:00 UTC and 11:00 UTC, with *CF* lower than 90%, but for less than one hour, so that they are included in the LLSC lifetime. For this case, T_b is at 12:05 UTC.

3.3 LWP budget

The equation of LWP tendency is based on the assumption of a horizontally-homogeneous stratocumulus and vertically well-mixed by the convective turbulent mixing which is driven by the cloud-top radiative cooling. Following van der Dussen et al. (2014) this equation can be split into five relevant processes:

$$\frac{\partial \mathrm{LWP}}{\partial t} = \mathrm{BASE} + \mathrm{ENT} + \mathrm{PREC} + \mathrm{RAD} + \mathrm{SUBS} \quad (1)$$

in which

$$\mathrm{BASE} = \rho\eta(\overline{w'q_t'}^{b} - \Pi\gamma\overline{w'\theta_l'}^{b}) \quad (1.a)$$

$$\mathrm{ENT} = \rho w_e(\eta\Delta q_t - \Pi\gamma\eta\Delta\theta_l - h\Gamma_{ql}) \quad (1.b)$$

$$\mathrm{PREC} = \rho\Delta P \quad (1.c)$$

$$\mathrm{RAD} = \rho\eta\gamma\Delta F_{rad} \quad (1.d)$$

$$\mathrm{SUBS} = -\rho h\Gamma_{ql} w_{s,CTH} \quad (1.e)$$

representing the effects of turbulent moisture and heat fluxes at the cloud base (BASE), evaporation or condensation caused by entrainment of ambient air from aloft (ENT), precipitation formation (PREC), radiative budget along the cloud layer (RAD) and large-scale subsidence (SUBS) at its cloud top.

In the above equations (1.a) to (1.e), $\overline{w'q_t'}^{b}$ and $\overline{w'\theta_l'}^{b}$ are respectively the total moisture specific humidity (q_t) and liquid-water potential temperature (θ_l) heat fluxes at the cloud base (superscript "b"), ρ is the mean air density over the cloud layer and h is the cloud depth. ΔF_{rad} and ΔP are the differences, in net radiation and precipitation respectively, between the cloud

top and base heights (van der Dussen et al., 2014). $\Delta\theta_l$ and Δq_t are the jumps of respectively θ_l and q_t across the cloud layer. w_e and $w_{s,CTH}$ are the cloud top entrainment and large scale subsidence velocities, respectively.

The equations also introduce the following parameters: the Exner function $\Pi = \left(\frac{P}{1000}\right)^{\frac{R_d}{C_p}}$; the adiabatic lapse rate of liquid water content $\Gamma_{ql} = g\eta\left(\frac{q_s}{R_d\overline{T}} - \frac{\gamma}{C_p}\right)$; $\gamma = \frac{L_v q_s}{R_v \overline{T}^2}$ and $\eta = \left(1 + \frac{L_v\gamma}{C_p}\right)^{-1}$. In those parameters, P and $\overline{T}$ are respectively the pressure and temperature of the cloud layer, q_s is the saturation water vapour specific humidity at P and $\overline{T}$. R_d and R_v are respectively the dry air and water vapour gas constant, L_v is the vaporization latent heat of water, C_p the specific heat of dry air at constant pressure, and g is the gravitational acceleration.

For our analysis of DACCIWA cases, we consider the LWP budget in early morning, and use the 05:00 UTC radiosounding, the ceilometer and the cloud radar measurements to estimate some terms of equation (1). In fact, this is the optimized time for the assumption of horizontally homogeneous and vertically well-mixed LLSC layer. The term PREC is supposed to be close to zero because no significant rain was measured at surface for the selected cases. The BASE term is not estimated because the turbulent fluxes at the LLSC base cannot be deduced from the available data set at Savè supersite. According to Pedruzo-Bagazgoitia et al. (2020), the term BASE is small at this time relatively to the three terms RAD, ENT and SUBS. The latter are the most significant contributions in early morning that we attempt to estimate.

The term RAD (Eq. 1.d) is retrieved from the vertical profiles of upwelling and downwelling radiative fluxes which are computed by using the Santa Barbara DISORT Atmospheric Radiative Transfer (SBDART) model (Ricchiazzi et al., 1998). This software tool, which solves the radiative transfer equation for a plane-parallel atmosphere in clear and cloudy conditions, was used in the studies of Babić et al. (2019a) and Adler et al. (2019) to estimate the temperature tendency due to radiative interactions during the LLSC diurnal cycle. For our simulations, the model configuration was very similar to that used in these studies. We prescribed 65 vertical input levels with a vertical resolution of 50 m below 2 km a.g.l, 200 m between 2 and 5 km a.g.l, and, 1 km above 5 km a.g.l. The vertical profiles of air pressure, temperature and water vapour density as well as the integrated water vapour are based on 05:00 UTC standard radiosounding data. The cloud optical thickness, which varies with its water and ice content, is required to describe a cloud layer in the SBDART model. Yet, the LWP provided by the microwave radiometer deployed at Savè supersite (Wieser et al., 2016) includes all the existing cloudy layers, and also is not available for five of our selected cases. Therefore, the LLSC optical thickness is determined from a parameterized LWP (Eq. 2), by assuming an adiabatic cloudy layer in which the liquid water mixing ratio (q_l) increases linearly (van der Dussen et al., 2014; Pedruzo-Bagazgoitia et al., 2020). The downwelling longwave radiations from potential mid-level and high-level clouds may reduce the radiative cooling at the stratocumulus top (e.g. Christensen et al., 2013). However, the cloud layers above the LLSC (base, top and water content) cannot be precisely described in the SBDART model from the available data set. Thus, the higher clouds radiative effect is not directly included in our estimate of downwelling radiative fluxes, but it is partially taken into account through vertical profiles of temperature and relative humidity

given by the radiosonde. As the shortwave radiations are zero before the sunrise, only the longwave range, 4.5-42 µm with spectral resolution of 0.1µm (Babić et al., 2019a), was selected for radiative fluxes calculations. For all the cases, the vertical optical depth of ABL aerosol is fixed to 0.38, which corresponds to the average value of the measurements performed with a sun photometer in June and July 2016 at Savè.

$$\mathrm{LWP} = -\frac{1}{2}\rho\Gamma_{ql}h^2 \quad (2)$$

For the term ENT (Eq. 1.b), we use the parameterization of Stevens et al. (2005) to estimate w_e:

$$w_e = A * \frac{\Delta F_{rad}}{\Delta\theta_l} \quad (3)$$

in which A is a non-dimensional quantity representing the efficiency of the warming caused by the input of warmer free tropospheric air into the stratocumulus cloud layer by the buoyancy-driven eddies generated by cloud-top radiative cooling. ***A* varies with $\Delta\theta_l$, Δq_t, wind shear at the cloud top, surface turbulent fluxes and cloud microphysical processes via the buoyancy flux vertical profile (Stevens et al., 2005; Stevens, 2006). Despite the spatial and temporal variability of *A*, its value is generally fixed and treated as a constant parameter in several research studies (e.g. van Zanten et al., 1999; van der Dussen et al., 2014).** The used value of A found in the literature varies from one study to another. By considering the results of the LES made by Pedruzo-Bagazgoitia et al. (2020) on a DACCIWA case, just before sunrise, with $w_e \approx 4.5\ mm.s^{-1}$, $\Delta\theta_l \approx 4\ K$, a cloud-top longwave radiative cooling of around 43 W m^{-2}, and, $\rho \approx 1.13\ \mathrm{kg}.m^{-2}$ as the average value from the surface to 1000 m a.g.l (from 26 June 05:00 UTC sounding), we obtain $A \approx 0.5$. This means that the contribution of entrainment driven by convective turbulence to the heat budget at the cloud top is around two times smaller than that driven by the cloud-top radiative cooling. For simplicity and due to a lack of precise estimate, we assume here the same behaviour for all the DACCIWA cases, and consider $A = 0.5$ in our analysis.

The jumps in temperature $\Delta\theta_l$ and in total water content Δq_t are estimated from the soundings. We write $\theta_l = \theta - \frac{1}{\Pi}\left(\frac{L_v}{C_p}\right) q_l$, with θ as the potential temperature, whereas $q_t = q + q_l$. We define:

$$\Delta\varphi \approx \varphi^+ - \varphi^- \quad (4)$$

where φ can be either θ_l or q_t. φ^+ and φ^- are in theory the values of the variable φ just above and just below the cloud top respectively. Under the assumption of a well-mixed cloud layer, θ_l (q_t) is conserved through the cloud layer and increases (decreases) abruptly in the warmer (drier) ambient air right above (vanZanten et al., 1999). Thus, $\Delta\theta_l$ and Δq_t can be estimated from the vertical profiles of θ and q derived to the 05:00 UTC standard sounding. For ${\theta_l}^+$ and ${q_t}^+$, we consider the mean over the 100 m above CTH. For ${\theta_l}^-$ and ${q_t}^-$, we consider the sounding level just below CBH. In brief, we use:

$$\begin{cases} {q_t}^- = q_{t\,\{\text{below cloud top}\}} = q_{t\,\{\text{below cloud base}\}} = q_{\{\text{below cloud base}\}} \\ {\theta_l}^- = \theta_{l\,\{\text{below cloud top}\}} = \theta_{l\,\{\text{below cloud base}\}} = \theta_{\{\text{below cloud base}\}} \end{cases} \quad (5)$$

For the term SUBS (Eq. 1.e), we have no possibility of estimating precisely the large scale subsidence at the LLSC top. One possibility is to consider evaluations from models or re-analyses. However, we decided to discard this approach, because the subsidence profiles from regional simulations with Consortium for Small-Scale Modelling (COSMO) or from ERA-interim and ERA-5 reanalyses showed a very high temporal variability and a strong lack of

coherence among the different cases. According to the cloud-radar CTH estimates, the LLSC top is often stationary at the end of the stratus phases during DACCIWA. This feature has been observed (Adler et al., 2019; Babić et al., 2019a; Dione et al., 2019) but also simulated by Pedruzo-Bagazgoitia et al. (2020). Based on the LLSC top stationarity at the time of our LWP budget analysis, $w_{s,CTH}$ is estimated following Lilly (1968):

$$\frac{\partial CTH}{\partial t} = w_{s,CTH} + w_e \approx 0 \quad (6)$$

4 LLSC during the stratus phase

In this section, we document the *stratus* phase of the LLSC diurnal cycle. The aim is to analyze the way the cloud layer is coupled to the surface processes, and the possible impacts the coupling has on the cloud characteristics (macrophysical properties and LWP terms). During the DACCIWA field campaign, the sunrise occurred at Savè between 05:33 and 05:42 UTC (Kalthoff et al., 2018). According to Lohou et al. (2020), the *convective phase* starts between 07:30 and 09:00 UTC. Moreover, the last radiosonde released before the *convective phase* is performed at 06:30 UTC, consequently, the analysis in this section concerns the period from the LLSC formation (beginning of the *stratus phase*) to 06:30 UTC on day-D+1.

4.1 Coupled and decoupled LLSC

We first analyze the evolution of LLSC base height (CBH) and its link with the NLLJ core height and surface-based LCL along the *stratus phase* (Fig. 3). The CBH and LCL at the beginning of the *stratus phase* (Fig. 3a and b) are given by the diagnostic parameters CBH^m and LCL^M respectively when the LLSC forms, and the NLLJ core height is the hourly-averaged value at that time. For the end of the *stratus phase* (Fig. 3c and d), CBH, LCL and NLLJ are averaged between 04:00 and 06:30 UTC on day-D+1.

When the LLSC forms, its base is located within the NLLJ core, where the cooling driven by the horizontal advection is maximum (Adler et al., 2019; Dione et al., 2019; Lohou et al., 2020). Both the CBH and NLLJ core height range between 50 and 500 m a.g.l (Fig. 3a) and are a hundred meters above the surface-based LCL, except for one case (Fig. 3b). This means that the LLSC is decoupled from the surface when it forms.

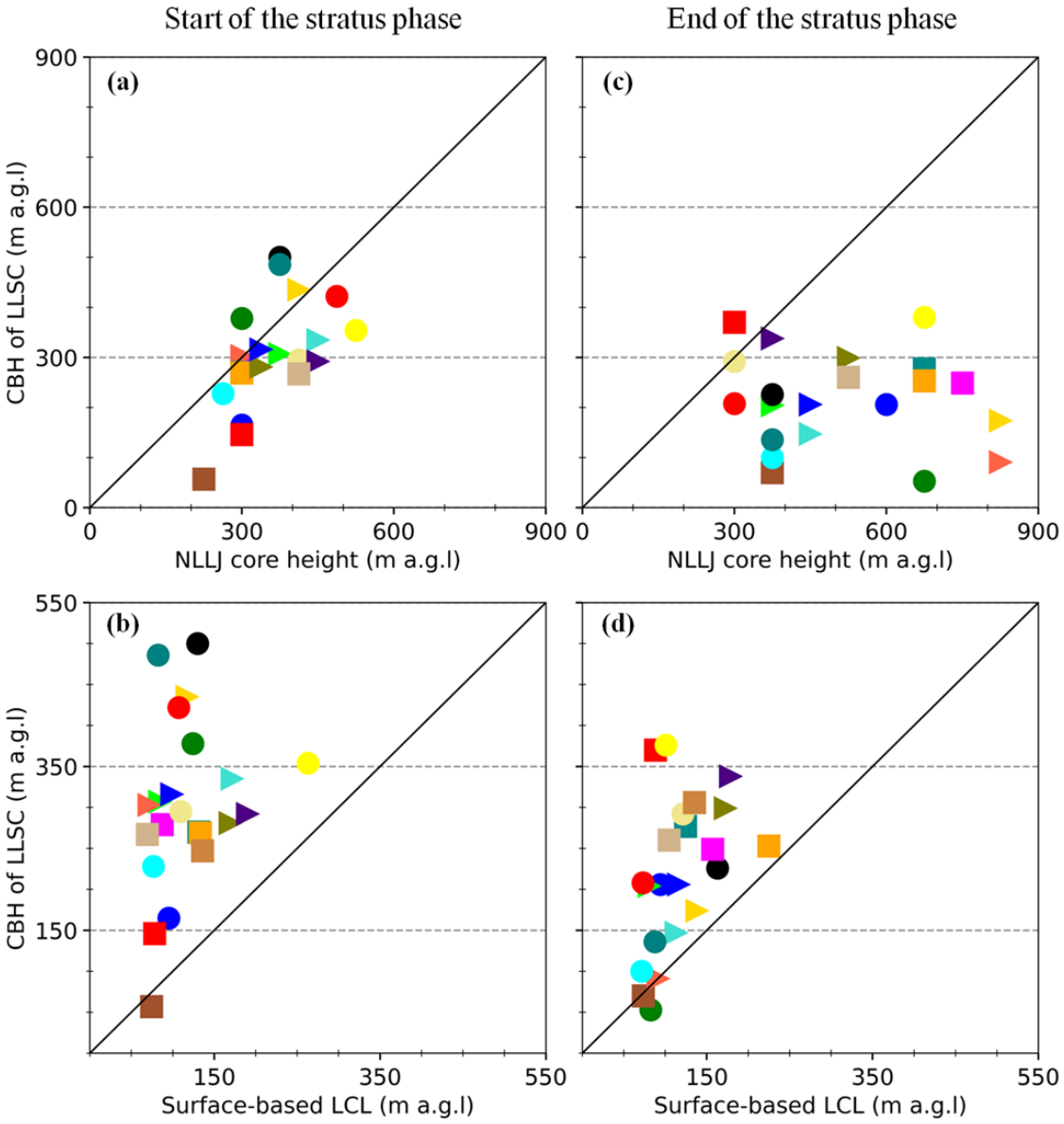

Figure 3 : LLSC base height (CBH) against the nocturnal low-level jet (NLLJ) core height (top panels), the surface-based lifting condensation level (LCL) (bottom panels), at the start **(a, b)** and at the end of *stratus phase* **(c, d)**. Each of the twenty-two selected cases is represented by a different marker.

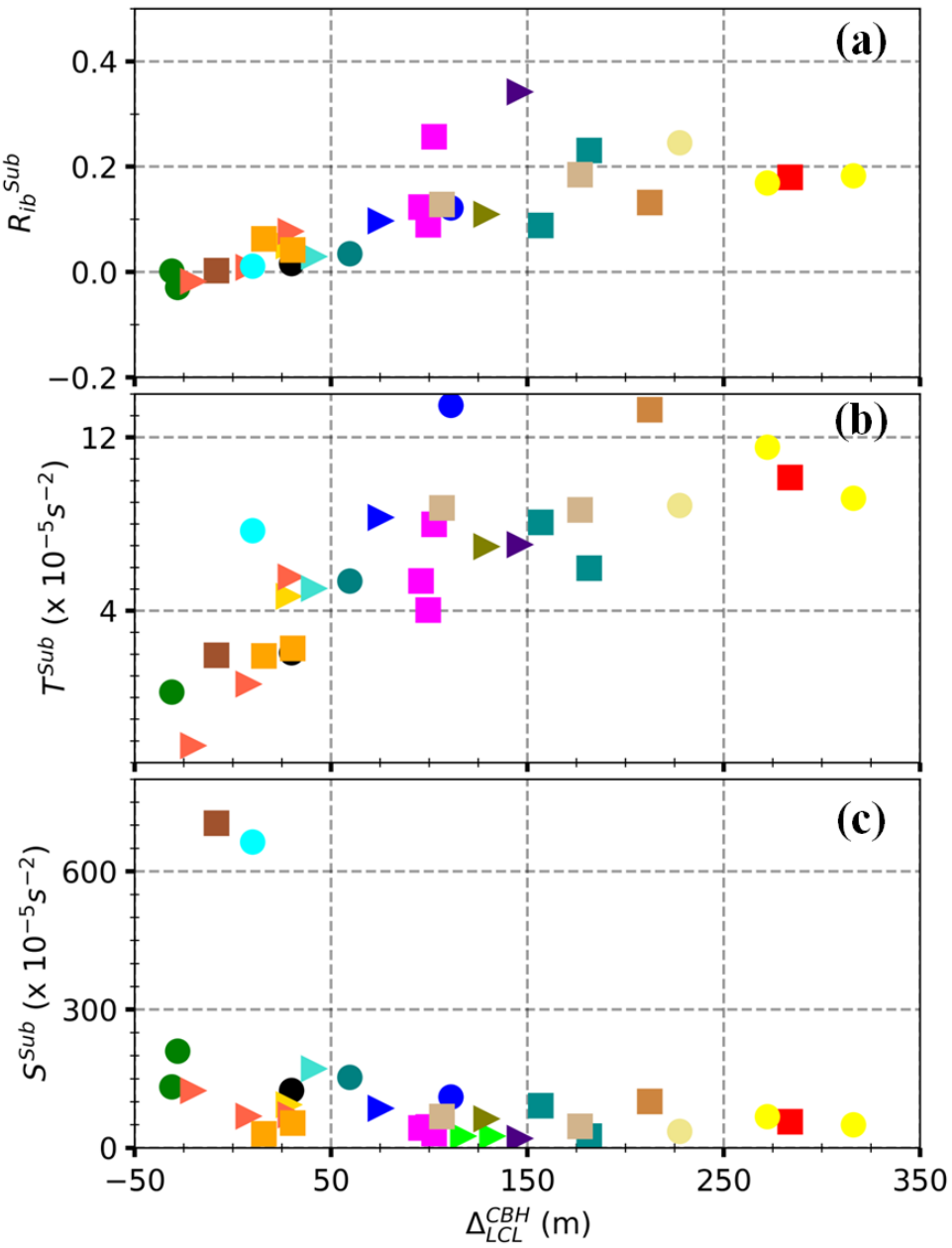

Figure 4 : Bulk Richardson number (R_{ib}^{Sub}, **a**), and its thermal (T^{Sub}, **b**) and vertical wind-shear (S^{Sub}, **c**) composing terms, as a function of the diagnostic parameter Δ_{LCL}^{CBH} which corresponds to the mean distance between the LLSC base height (CBH) and surface-based lifting condensation level (LCL), performed by using all radiosoundings available from 04:00 to 06:30 UTC on day-D+1 for each studied case. Each marker corresponds to one case.

At the end of the *stratus phase*, one can see that the relationship between CBH and the NLLJ core height has totally changed (Fig. 3c). There is no clear linear link between both, and CBH remains mostly lower than or equal to 300 m a.g.l, while the NLLJ core height is above 600 m a.g.l in several cases. This is most likely because, during the *stratus phase*, the jet axis is shifted upward by the convective turbulence within the LLSC layer (Adler et al., 2019; Dione et al., 2019; Lohou et al., 2020). In addition to the jet axis rising, the averaged CBH decreases by the end of the *stratus phase* (Fig. 3a and c) for most of the cases. In some cases, CBH coincides pretty well with LCL (Fig. 3d), which indicates a coupling of the LLSC with the surface at the end of the *stratus phase*. But, in others, CBH is still at least 100 m higher than LCL, meaning that the LLSC remains decoupled from the surface.

We further analyze the coupling between the LLSC and the surface by the end of the *stratus phase* by using the bulk Richardson number (Stull, 1988) of the subcloud layer (R_{ib}^{Sub}). It reads:

$$R_{ib}^{Sub} = \frac{T^{Sub}}{S^{Sub}} \text{ with } T^{Sub} = \frac{g}{\theta} * \frac{\Delta\theta}{CBH} \text{ and } S^{Sub} = \left(\frac{\Delta U}{CBH}\right)^2. \quad (7)$$

T^{Sub} and S^{Sub} are respectively the thermal and horizontal wind shear contributions to the Richardson number. $\frac{\Delta\theta}{CBH}$ and $\frac{\Delta U}{CBH}$ are the bulk vertical gradient of θ and horizontal wind speed (U) respectively within the subcloud layer (between the cloud base and the surface), with the assumption that U is null at the surface. R_{ib}^{Sub} is estimated with all radiosoundings available from 04:00 to 06:30 UTC on day-D+1, for each studied case. The subcloud layer height is estimated with the half-hourly median of CBH^{m} at the radiosonde released time (Eq. 7).

Figure 4 shows R_{ib}^{Sub} (Fig. 4a), T^{Sub} (Fig. 4b) and S^{Sub} (Fig. 4c) as a function of the half-hourly median value of Δ_{LCL}^{CBH} at the radiosonde released time. The smaller Δ_{LCL}^{CBH}, the lower R_{ib}^{Sub}. Interestingly, when Δ_{LCL}^{CBH} is smaller than 75 m, R_{ib}^{Sub} is less than or equal to 0.1 (Fig. 4a). This evidence suggests that the potential coupling between the LLSC and the surface during the *stratus phase* is driven by the underlying turbulent mixing. A similar tendency was found by Adler et al. (2019) who analyzed the soundings performed along the *stratus phase* of eleven IOPs.

As R_{ib}^{Sub}, the term T^{Sub} increases with Δ_{LCL}^{CBH}, whereas the term S^{Sub} is nearly constant. This means that, when the CBH is close to the LCL, the subcloud layer is well mixed, although the shear-driven turbulence is not particularly significant. Thus, the coupling between the LLSC and the surface at the end of the *stratus phase* seems to be mostly linked to the thermal stratification in the subcloud layer, rather than to the shear-driven turbulence.

Finally, based on Fig. 4 (a and b), the value of 75 m is used thereafter as a threshold for Δ_{LCL}^{CBH} to distinguish the coupled and decoupled LLSC at the end of the *stratus phase*. Through this classification, our set of twenty-two studied cases includes nine LLSC coupled to the surface (case C) and thirteen LLSC decoupled from the surface (case D) (Table A-1). Among the nine selected IOPs, three (N° 5, 6 and 8) and six (N° 3, 4, 7, 9, 11 and 14) are cases C and D respectively.

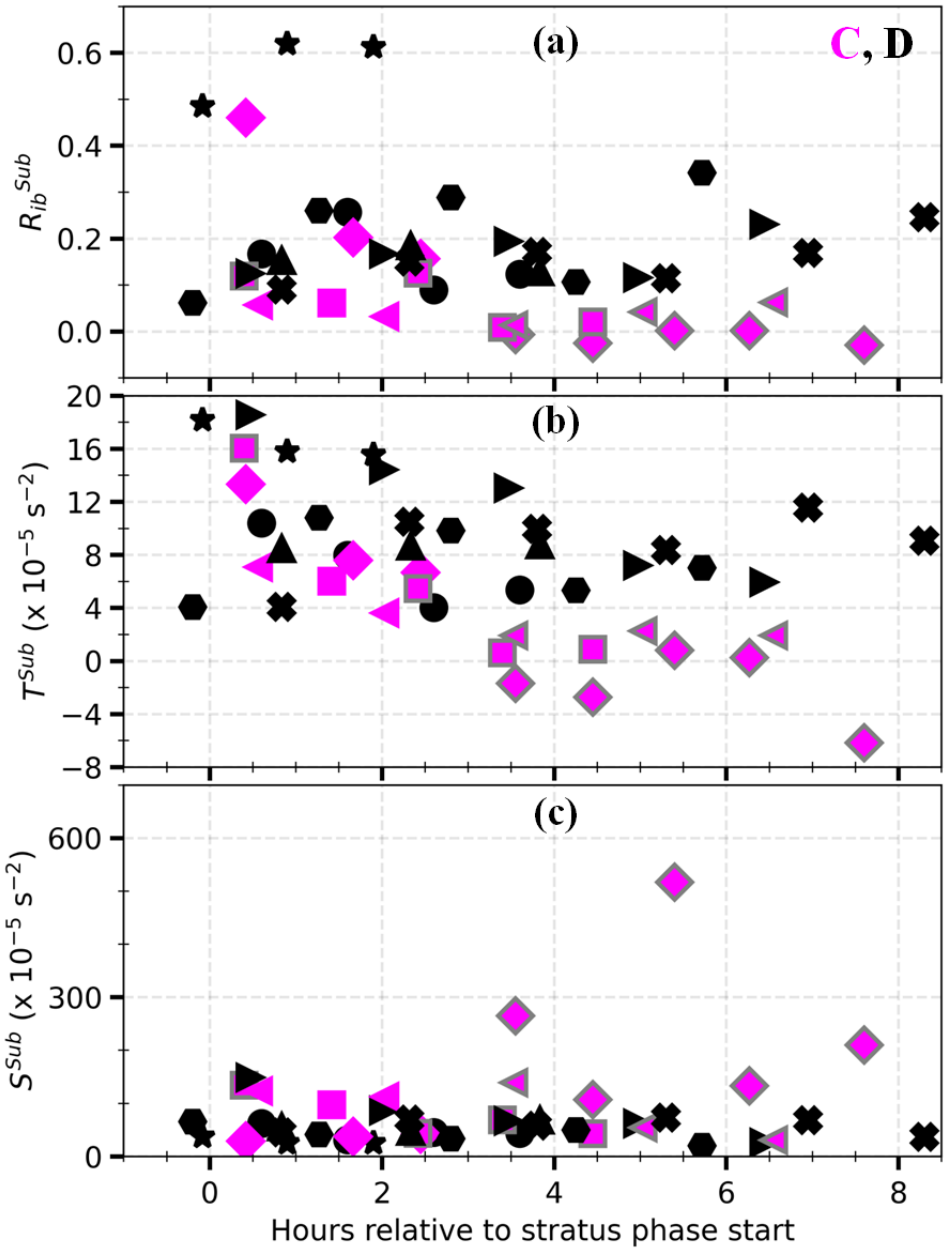

Figure 5 : Evolutions of the bulk Richardson number (R_{ib}^{Sub}, **a**) and its thermal (T^{Sub}, **b**) and vertical wind-shear (S^{Sub}, **c**) composing terms during the stratus phase, based on all the soundings available until 06:00 UTC on day-D+1 during the nine selected IOPs (Table A-1). The quantities are presented against the radiosonde released time which is expressed in hours relative to the start of the stratus phase. Each IOP is represented by a marker. C and D stand for the coupled and decoupled LLSC at the end of the stratus phase respectively. The grey edge indicates that the mean distance between the LLSC base height and the surface-based lifting condensation level (LCL) (Δ_{LCL}^{CBH}) is of less than 75 m at the sounding time, meaning that the cloud is coupled to the surface.

Based on the re-usable radiosoundings available for the nine selected IOPs, the temporal evolution of R_{ib}^{Sub} and its composing terms have been calculated from the start of the *stratus phase* up to 06:30 UTC on day-D+1 (Figure 5). R_{ib}^{Sub}, T^{Sub} and S^{Sub} in cases C and D are similar when the LLSC forms. For cases C, T^{Sub} decreases down to zero (neutral stratification) within the three following hours while S^{Sub} remains almost constant, which causes a decrease of R_{ib}^{Sub} (Fig. 5a and b). In the cases C presented in Fig. 5, the definitive coupling with the surface occurs within the four hours after the beginning of the *stratus phase*. The same behaviour is observed for the cases C which are not IOP and therefore not included in Fig. 5 (not shown). For cases D, the subcloud layer remains thermally stable along the *stratus phase* and the shear-driven turbulence is of the same order than for cases C. Considering these results, it appears that the shear-driven turbulence in the subcloud layer is not the main process which causes the LLSC coupling with the surface during the *stratus phase* in the cases C.

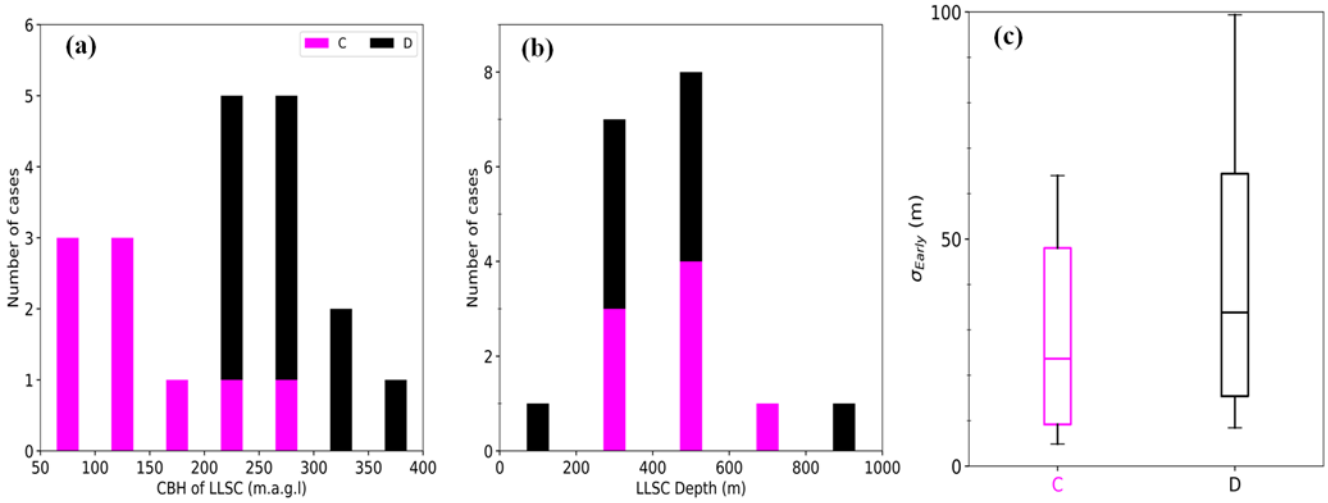

Figure 6 : Statistic on the LLSC macrophysical characteristics at the end of the *stratus phase*, performed on the twenty cases (the nine cases C and eleven cases D out of thirteen), for which the LLSC is present (CF ≥ 90%) over at least 70% of the time between 04:00 and 06:30 UTC on day-D+1. Distributions of, LLSC base height (CBH, **a**), the same than on Figure 3, and depth **(b)**, calculated by using the median value between 04:00 and 06:30 UTC of cloud-radar estimated CTHs as the LLSC summit. The depth was not estimated for two cases (one C and one D) among the twenty due to CTHs missing data. Statistical information on σ_{Early} **(c)**, which is the median value between 04:00 and 06:30 UTC of the diagnostic parameter σ^*, measuring the homogeneity at the LLSC base. The edges of the boxes represent the 25^{th} , the median and 75^{th} percentiles, and the whiskers, the minimum and the maximum values. C and D stand for the coupled and decoupled LLSC respectively.

In conclusion, the LLSC forms typically decoupled from the surface. Subsequently, its base lowers during the first hours of the *stratus phase*. In the cases C, this decrease is more important and leads to the coupling between the cloud and the surface before the sunrise. The lowering of the LLSC base was first pointed out by Babić et al. (2019a) for the 07-08 July case. They explained this feature by an additional cooling in the subcloud layer mainly due to a shear-driven turbulent mixing caused by the NLLJ. Yet, no substantial differences in wind shear below the LLSC are observed between the cases C and D, indicating that the processes related to the mechanical turbulence underneath the LLSC cannot fully explain the coupling observed by the end of the *stratus phase*. The other relevant processes which may couple the LLSC to the surface in night-time conditions are discussed in section 4.3. In the next paragraph, we analyze the LLSC macrophysical characteristics in the C and D cases at the end of the *stratus phase*, i.e. just before the *convective phase*.

The distributions of averaged LLSC base height, CBH, and depth at the end of the *stratus phase* are summarized in Fig. 6a and b respectively. Only the twenty cases for which the cloud is persistent between 04:00 and 06:30 UTC on day-D+1 are considered (including nine cases C and eleven cases D). Note that the depth could not be estimated for two of these cases because of CTH missing data. The CBH ranges within 50-200 m a.g.l for cases C, and within 200-400 m a.g.l for cases D. This clear difference between coupled and decoupled LLSC explains the bimodal distribution of morning CBH observed by Kalthoff et al. (2018). In contrast, the morning LLSC depth does not depend on the state of coupling with the surface.

Figure 6c helps to study the LLSC base homogeneity at the end of the *stratus phase* by presenting the statistical information of σ_{Early}, which is the median value of the diagnostic parameter σ^* between 04:00 and 06:30 UTC on day-D+1 for each considered case. The median of σ_{Early} is 24 m for cases C and 34 m for the cases D. Their 25^{th} percentiles and minimums are close, but, the 75^{th} percentile for cases D is more than 15 meters higher than that of cases C, and the maximum is significantly larger, close to 100 m. This reveals the larger LLSC base heterogeneity found for several cases D. Likely, the coupling with the surface limits the fragmentation of the LLSC layer, and helps maintaining the homogeneity of the cloud in cases C.

In brief, the mechanism of coupling favours lower CBH and slightly more homogeneous cloud base in the cases C. But the LLSC depth is similar in cases C and D, so that the LLSC vertical extension does not seem to be influenced by the coupling with the surface. This may be related to the negligible contribution of surface fluxes during the night.

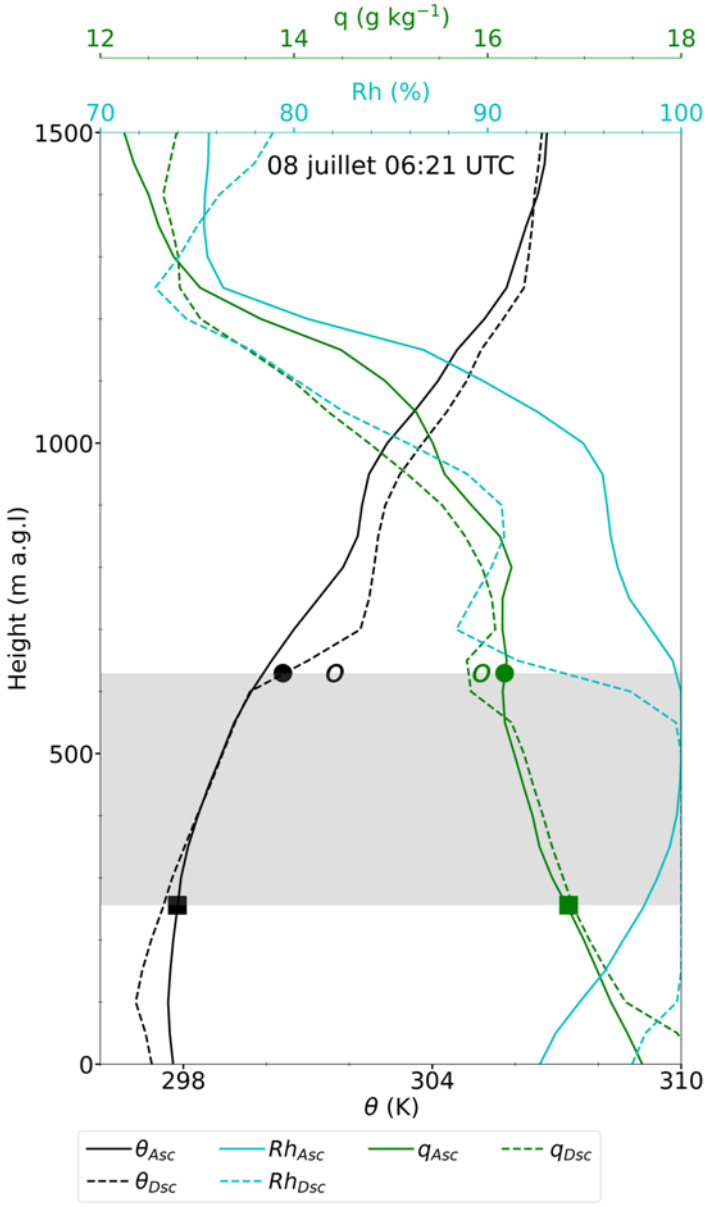

Figure 7 : Vertical profiles of the low-troposphere acquired by the re-usable radiosonde of 08 July 2016 at 06:21 UTC, when the probe ascents ('Asc', filled line) and descends ('Dsc', dashed line). The variables shown are the relative humidity (Rh), the potential temperature (θ) and the water vapour specific humidity (q). The shaded grey delimits the LLSC layer, based on the ceilometer and cloud-radar measurements. The values of φ^{+}(φ^{-}) (Eq. 4) for θ and q are marked with dot (square). The filled symbols correspond to the ascent, whereas the unfilled symbols correspond to the descent.

4.2 LWP terms

In order to deepen the analysis, we make an attempt to estimate the LWP terms at the end of the *stratus phase*. Several questions motivate this attempt:

1) Do we find similar results with observations and with previous numerical simulations, particularly that of Pedruzo-Bagazgoitia et al. (2020)?

2) Does the LWP budget analysis help us to differentiate the cases C and D?

As previously seen, the most important contributions in the LWP budget are that of radiation, entrainment and subsidence. Based on the available observations and by using the SBDART model, we estimate ENT and RAD (Eq. 1.b and d respectively), and also give a rough magnitude order of SUBS (Eq. 1.e). The LLSC layer here is defined by the averaged CBH and CTH at the end of the *stratus phase* (Fig. 6a and b).

We first discuss the jumps Δq_t and $\Delta \theta_l$ across the cloud top (Eq. 4 and 5), which are involved in ENT and RAD terms. They are estimated by the use of the 05:00 UTC (day-D+1) standard radiosoundings. **The liquid water buildup on the probe sensors possibly renders some measurements suspect, especially at the exit of the cloud.** In order to evaluate the impact of this issue on our jump estimations from the 05:00 UTC standard radiosonde, we first consider a re-usable sounding at a different time, for which the probe has crossed the LLSC layer both at ascent and descent. At ascent, the sensor is reliable at cloud base, but may get wrong data when it reaches cloud top. At descent, it is the reverse: correct at cloud top but possibly erroneous measurements when it reaches cloud base. This is shown in Fig. 7, which displays the vertical profiles of θ, q and Rh measured by the re-usable sounding of 08 July 2016 at 06:21 UTC, during both the probe ascent and descent. By analyzing the Rh vertical profiles, one can see that the upper limit of the saturated layer (Rh <= 98.5), i.e. LLSC layer top, obtained by the descent measurements is more consistent with the cloud-radar-estimated CTH than that obtained during the ascent. Further, the descent measurements indicate warmer and drier atmospheric conditions from the CTH to around 800 meters above, with θ^+ (q^+) around 1 K (0.3 g kg^{-1}) higher (smaller). By analysing all re-usable soundings of that kind during daytime, we find that the maximum underestimation (overestimation) of θ^+ (q^+) during the ascent due to the wetting of the sensors is about 1.2 K (0.3 g kg^{-1}). The overestimation of q^+ by the ascending sounding is within the measurement accuracy. While, compared to the 0.2° C measurement accuracy, the underestimation of θ^+ is significant. Consequently, we only consider a systematic error of 1.2 K on the estimates of θ^+ from the 05:00 UTC standard radiosounding, for which we can only rely on the ascent (the descent is too far away from the supersite).

Figure 8 displays Δq_t and $\Delta \theta_l$ against q^- and θ^- respectively, as estimated for the fourteen cases (eight cases C and six cases D) among the twenty cases of Figure 6, for which there is evidence that the radiosonde flew throughout the LLSC layer. It first reveals that the thermodynamical conditions of the subcloud layer are quite steady during this summer period, with only 1.5 g kg^{-1} and 2 K variation range for humidity and temperature, respectively, over all the cases. Similar

conclusion was found by Adler et al. (2019). This may be due to the fact that the considered cases occurred in nearly similar synoptic conditions over SWA (Table A-1).

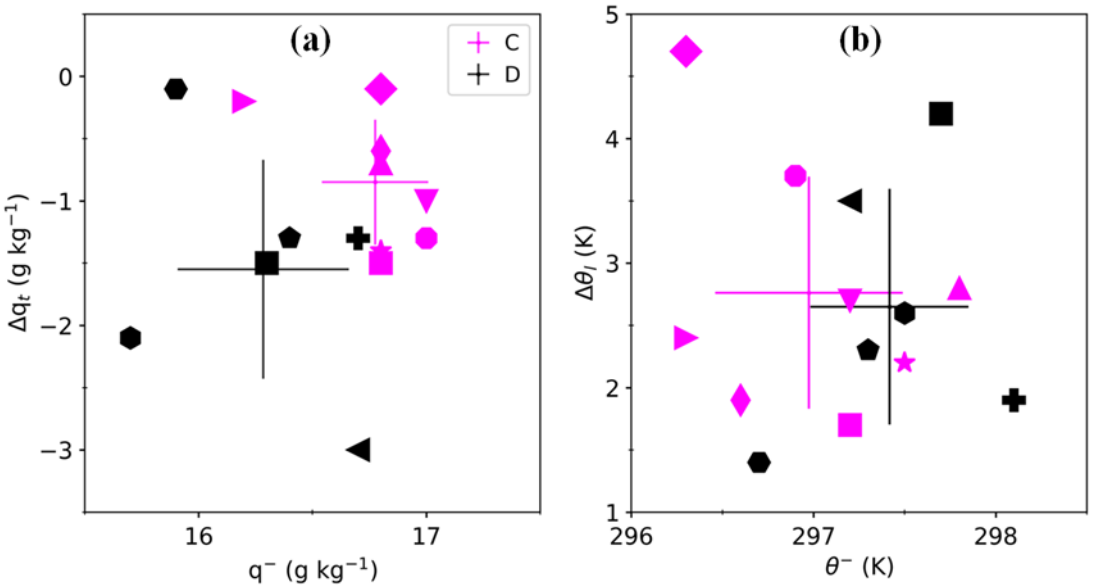

Figure 8 : Humidity jump at the LLSC top (Δq_t) against specific humidity at the LLSC base q^-**(a)**, temperature jump at the LLSC top $\Delta\theta_l$ (possible underestimation of around 1.2 K) against potential temperature at the LLSC base θ^-**(b)**, derived from the fourteen 05:00 UTC standard morning soundings for which the probe flew within the LLSC layer (Table A-1). In each panel, the error bars correspond to the standard deviation, and cross at the mean over all C (magenta) or D (black) cases. Each symbol represents a single case.

In the cases C, q^- ranges within the interval 16-17 g kg^{-1}, with a mean of 16.8 g kg^{-1} and a standard deviation of 0.5 g kg^{-1}. It is lower in the cases D, with an average of 16.3 g kg^{-1} and a standard deviation of 0.9 g kg^{-1}. Thus, in early morning, the air just below the LLSC is in average 0.5 g kg^{-1} moister in the cases C. This is qualitatively true for the entire *stratus phase*, when analyzing the re-usable soundings of the nine IOPs (not shown). Δq_t is overall in absolute lower than 3.0 g kg^{-1}. It is smaller than or equal to 1.5 g kg^{-1} for 85% of all the cases. This indicates a generally weak moisture jump across the LLSC top. This is still more pronounced in the cases C, for which Δq_t remains lower than 1.5 g kg^{-1} in absolute.

The parameter θ^- ranges within 296-299 K. Beyond the same variability found in cases C and D, θ^- is in average around 0.5 K cooler in the cases C, probably because of closer LLSC base to the surface. $\Delta\theta_l$, which varies within the interval 1-5 K, does not exhibit a clear difference between the cases C and D. Thus, the fact that the LLSC base gets closer to the surface in the cases C does not impact the temperature jump across the LLSC top.

The magnitude of $\Delta\theta_l$ and Δq_t observed in SWA conditions are much smaller than those typically found for the mid-latitude stratocumulus, which can be as strong as 10 K and -10 g kg^{-1} (Duynkerke et al., 2004; Wood, 2012; van der Dussen et al., 2016; Ghonima et al., 2016), especially over the ocean. The vertical profile used by Pedruzo-Bagazgoitia et al. (2019) to initialize their LES had a $\Delta\theta_l$ of 4.5 K and no humidity jump across the LLSC layer. This representation is consistent with what we find for the moisture jump, but is on the sidelines for the temperature jump.

Table 1 : Median and standard deviation of some parameters in the RAD, ENT and SUBS formulation estimated from the fourteen 05:00 UTC radiosoundings presented in Figure 8. The standard deviation (in brackets) over the cases is not indicated when it is negligible. Our results are compared with the values used in van der Dussen et al. (2014).

	Order of magnitude	
Parameters	DACCIWA cases	Study case of van der Dussen et al. (2014)
$\overline{T}$	294 (0.7) K	283 K
$\bar{q}$	16.2 (0.5) g kg^{-1}	8.2 g kg^{-1}
$\rho C_p \Delta F_{rad}$	55 (5) W m^{-2}	48 W m^{-2}
γ	~1.012 g kg^{-1} K^{-1}	0.55 g kg^{-1} K^{-1}
η	~ 0.28	0.42
Γ_{ql}	~ -2.29 g kg^{-1} km^{-1}	-1.86 g kg^{-1} km^{-1}
w_e	10.12 (2.53) mm s^{-1}	--

Table 1 compares our estimates of some parameters involved in the formulation of RAD, ENT and SUBS terms with those of van der Dussen et al. (2014) study case, which are based on the DYCOMS-II (Second Dynamics and Chemistry of Marine Stratocumulus field study) case setup (Stevens et al., 2005). The quantities γ, η, and Γ_{ql} differ from the typical values used by these authors because the cloud layer is in average 11 K warmer and 8 g kg^{-1} wetter in our case. For these three parameters, the standard deviation over the fourteen cases is lower than 3% of the median. After the analysis of the SBDART model output, ΔF_{rad} is determined from the difference of the net radiative fluxes between the model levels just above and below the LLSC layer respectively. The median and the standard deviation of cloud-top longwave radiative cooling are respectively about of 55 and 5 W m^{-2}. Our estimate of the radiative cooling at the LLSC top for the 25-26 June 2016 case is 44.6 W m^{-2} (Table A-1), which is in good agreement with the value of 43 W m^{-2} estimated in Pedruzo-Bagazgoitia et al. (2020) LES for the same day just before the sunrise. Despite weaker temperature and nearly absent moisture jumps at the LLSC top, the median value of our estimated cloud-top radiative cooling is around 10 W m^{-2} greater

than the one of van der Dussen et al. (2014) and fits within 50-90 W m^{-2} which is the typical interval range found for the subtropical stratocumulus (Wood, 2012). This is most likely because our LLSC is significantly warmer.

We find only a 5 W m^{-2} standard deviation for the radiative cooling at the LLSC top and no particular difference between cases C and D. This very low standard deviation may be due to the conditions which remained very steady from one case to the other, but may also be underestimated because the impact of higher clouds are not fully included in the radiative fluxes estimate. In order to evaluate the error due to the temperature underestimation above the LLSC top, SBDART is run with the measured and a corrected temperature profile, while the other inputs remain unchanged. The correction of the potential temperature vertical profile consists in a linear tendency between the measured θ plus a 1.2K correction right above the CTH and the measured θ at 800 m, where we consider that the radiosonde sensor is no more affected by the LLSC crossing. The cloud-top radiative cooling estimated by SBDART with this corrected temperature vertical profile is larger by less than 2 W m^{-2}.

The cloud-top entrainment velocity, w_e (Eq. 3), has a median value of 10.12 mm s^{-1} and its variability is around 25% of the median. This median is around 2.5 times higher than the velocity obtained by Pedruzo-Bagazgoitia et al. (2020) with LES and among the highest values found by other authors (Duynkerke et al., 2004; Faloona et al., 2005; Mechem et al., 2010; Ghonima et al., 2016). Finally, this discussion shows that our estimates of RAD and ENT are suitable, beyond the potential errors on the entrainment efficiency, *A*, and the simplified settings in SBDART. As mentioned in section 3.3, we approximate SUBS with the assumption of stationary LLSC top at the sounding time (Eq. 6). This term has to be taken with more caution than the two other terms, due to this hypothesis.

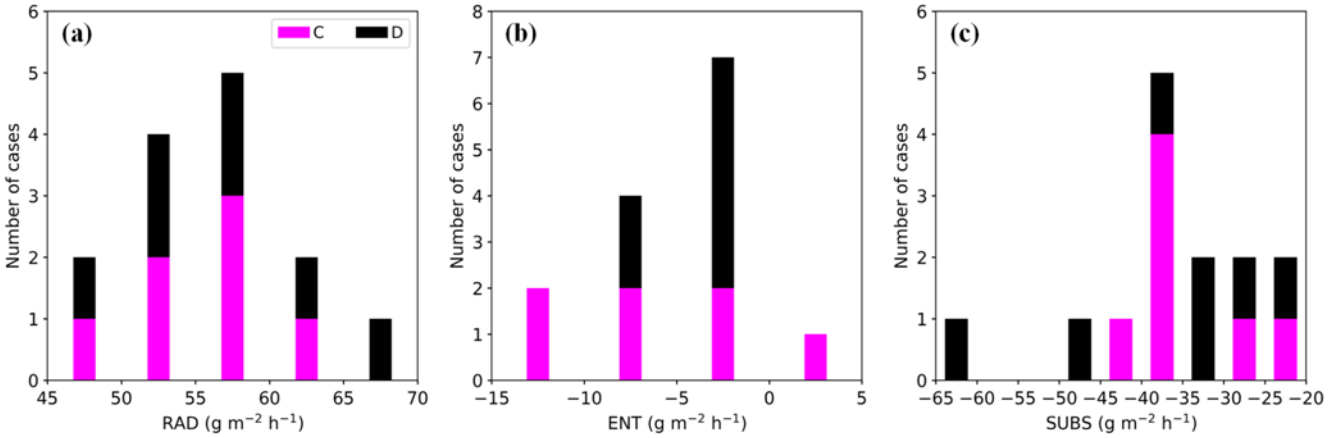

Figure 9 : Distributions of radiative (RAD, a), entrainment (ENT, b) and large scale subsidence (SUBS c) LWP budget terms (Eq. 1), derived from the fourteen 05:00 UTC standard soundings at Savè supersite for which the probe crossed into the LLSC layer (Fig. 8 and Table A-1). The methodology is described in section 3.3.

Figure 9 presents the distributions of RAD (Fig. 9a), ENT (Fig. 9b) and SUBS (Fig. 9c) derived from the fourteen radiosoundings considered in Fig. 8 by the methodology described in section 3.3. The RAD term ranges within 45-70 g m^{-2} h^{-1}, with a median of 57 g m^{-2} h^{-1}. ENT varies between -15 and 5 g m^{-2} h^{-1}, indicating a smaller contribution to the LWP budget compared to RAD. The negative value of about -10 is consistent with the study of Pedruzo-Bagazgoitia et al. (2020), with a predominant role of cloud-top temperature and humidity jumps and a drying and warming effect of the entrainment. Among the fourteen cases, several have a smaller contribution of ENT than this. One case even has a positive value for ENT, which means that the LLSC depth has more impact than the temperature and humidity jumps, so that the entrainment in that case favours the LLSC deepening. The term SUBS ranges between -65 and -20 g m^{-2} h^{-1}, with a median of around -36 g m^{-2} h^{-1}. It corresponds to as much as -0.4 to -0.9 times the RAD term, which is very significant. This is also consistent with Pedruzo-Bagazgoitia et al. (2020) who found the ratio SUBS/RAD approximately equals to -0.4 before sunrise. Our answers to the two questions raised at the start of this section are:

1) We found similar results compared to Pedruzo-Bagazgoitia et al. (2020). However, the West African inland LLSC layer, which develops within the monsoon flow (Dione et al., 2019), is characterized by weaker temperature and humidity jumps, but with similar radiative cooling at its top compared to marine stratiform clouds.

2) The cloud-top radiative cooling and the three LWP terms RAD, ENT and SUBS do not exhibit significant differences between the cases C and D, because of similar cloud depth and thermodynamic characteristics. The slight differences in CBH and moisture jump across the cloud top between the two types of cases do not impact the cloud-top radiative cooling and the LWP budget analysis at the end of the *stratus phase*.

By a series of sensitivity tests based on horizontal wind speed profiles, Pedruzo-Bagazgoitia et al. (2020) found that a wind shear at the cloud top before the sunrise, as such observed for the LLSC during DACCIWA (Lohou et al., 2020), may accelerate the cloud deck breakup during the *convective phase*, by generating dynamical turbulence which enhances the term ENT. However, they did not investigate the effect of wind shear underneath the LLSC.

From the fourteen morning soundings considered in Fig. 8, we quantified the contribution of vertical shear to the production of turbulence at the LLSC top (Table A-1). We find it to be generally smaller than 20.10^{-5} s^{-2}, that is considerably smaller than the one imposed at the initialization of the LES experiments performed by Pedruzo-Bagazgoitia et al. (2020). However, this contribution in the subcloud layer is mostly higher than 50.10^{-5} s^{-2} (Fig. 4c). Thus, the dynamical instability induced by the NLLJ is more important below the LLSC than above. This should imply that the mechanical turbulence driven by the NLLJ impacts much more the turbulent fluxes at the LLSC base than the entrainment of ambient air from above.

4.3 Factors controlling the coupling

From previous studies, several processes may lower the LLSC base and couple it with the surface during the *stratus phase*: (i) the shear-driven turbulence in the subcloud layer (Adler et al., 2019; Babić et al., 2019a), (ii) the cloud droplet sedimentation at the cloud base (Dearden et al., 2018), (iii) the light precipitation formation, i.e. drizzle (Wood, 2012), (iv) the convective overturning driven by the cloud-top radiative cooling (Wood, 2012), and, (v) large scale advection (Zheng and Li, 2019). Sections 4.1 and 4.2 allowed us to test several of these hypotheses to understand why the LLSC couples to the surface in some cases during DACCIWA.

As discussed in section 4.1, there is no difference in shear-driven turbulence between cases C and cases D which could explain the thermally neutral stratification of the subcloud layer in cases C and the stable stratification in cases D. So, the NLLJ does not seem responsible for the coupling in the cases C.

With LES experiments based on the 04-05 July case (case D, IOP7), Dearden et al. (2018) hypothesized that the LLSC base descent during the night is due to the cloud droplets sedimentation at the cloud base. However, the cloud base decrease is of less than 50 m before the sunrise in this numerical experiment, whereas the observed LLSC base descent is larger than 100 m by the end of the *stratus phase* in most of our studied cases, either C or D. Thus, the cloud droplets sedimentation should not explain by its own the coupling in cases C.

For all the studied cases, no precipitation was recorded at the surface during the *stratus phase*. However, drizzle formation below the LLSC base can hardly be measured by rain-gauge sensors. So, this hypothesis cannot be fully verified and remains a possibility. Concerning the radiative cooling at the LLSC top, section 4.2 shows that this positive contribution to the LWP budget at the end of the *stratus phase* is similar in cases C and D.

The large scale effects must be considered in the LLSC formation (Babić et al., 2019b), but also in its diurnal cycle. Indeed, eight of the nine cases C are observed between the 26 June and 8 July 2016 (Table A-1). This period corresponds to the first days of the post-onset phase characterized by a well-established and undisturbed monsoon flow over SWA (Knippertz et al., 2017). Warmer advection was observed to decouple stratiform cloud from the surface (Zheng and Li, 2019). Therefore, the reverse process, i.e. cooler advection, may produce the opposite effect. This hypothesis is all the more likely since the LLSC formation during the West African monsoon season is mainly due to a cooler air horizontal advection. The res-usable soundings performed during the *stratus phase* of the nine IOPs revealed that, at 50 m a.g.l (sounding level below the lowest CBH at the end of the *stratus phase*), the relative humidity remains larger than 90% for all the cases (not shown). For cases C, a decrease of the specific humidity (by around 1 g kg^{-1}) and a slight decrease of temperature (by around 0.2 °C) are observed between the LLSC formation and its coupling, which maintains Rh constant. However, no clear tendency was observed in the cases D. The very small temporal tendency of the temperature and humidity and the small number of studied cases do not allow us to definitively conclude on the effect of cooling and drying due to horizontal advection of the maritime inflow. However, this advection seems to persist in cases C and could have some impacts. If not on the LLSC base lowering (because Rh

is constant at 50 m a.g.l), the dry advection can have an effect on the LCL evolution. Indeed, a 1 g kg^{-1} decrease of near-surface specific humidity implies an elevation of surface-based LCL by a hundred meters, which facilitates the coupling.

It emerges from the above discussion that none of the processes listed at the beginning of this section is solely responsible for the coupling. We can hypothesize that it is the combination of several of those processes, each with a small impact, which leads to the LLSC coupling with the surface. After the coupling, the turbulence underneath has a crucial role for its maintenance during the rest of the *stratus phase*, as indicated by the reduction of thermal stability in the subcloud layer for the cases C (Fig. 5b). Indeed, the contributions of the shear-driven turbulence below the NLLJ and the turbulence due to the radiative cooling at the cloud top are important for mixing potential temperature in the subcloud layer (Dione et al., 2019; Lohou et al., 2020). In the LES experiments under windless conditions carried out by Pedruzo-Bagazgoitia et al. (2020), the cloud-top radiative cooling was the unique source of turbulence in the ABL until sunrise, and the coupling between the cloud and the surface was maintained.

5 Evolution of the LLSC layer under daytime conditions

In this section, the evolution of the LLSC during the *convective phase* until its breakup is analyzed.

5.1 The three scenarios of evolution

The evolution of LLSC during the *convective phase* is first analyzed according to the ceilometer-derived CBHs temporal change relatively to the surface-based LCLs. From this point of view, all the cases C evolve quite similarly during this phase, while two distinct scenarios are observed among the cases D (hereafter named DC for “decoupled-coupled” and DD for “decoupled-decoupled”). Each of the three scenarios is illustrated by one typical example; the LLSC occurrence on 07-08 July (Fig. 10a) for scenario C, 25-26 June (Fig. 10b) and 04-05 July (Fig. 10c) for scenarios DC and DD respectively.

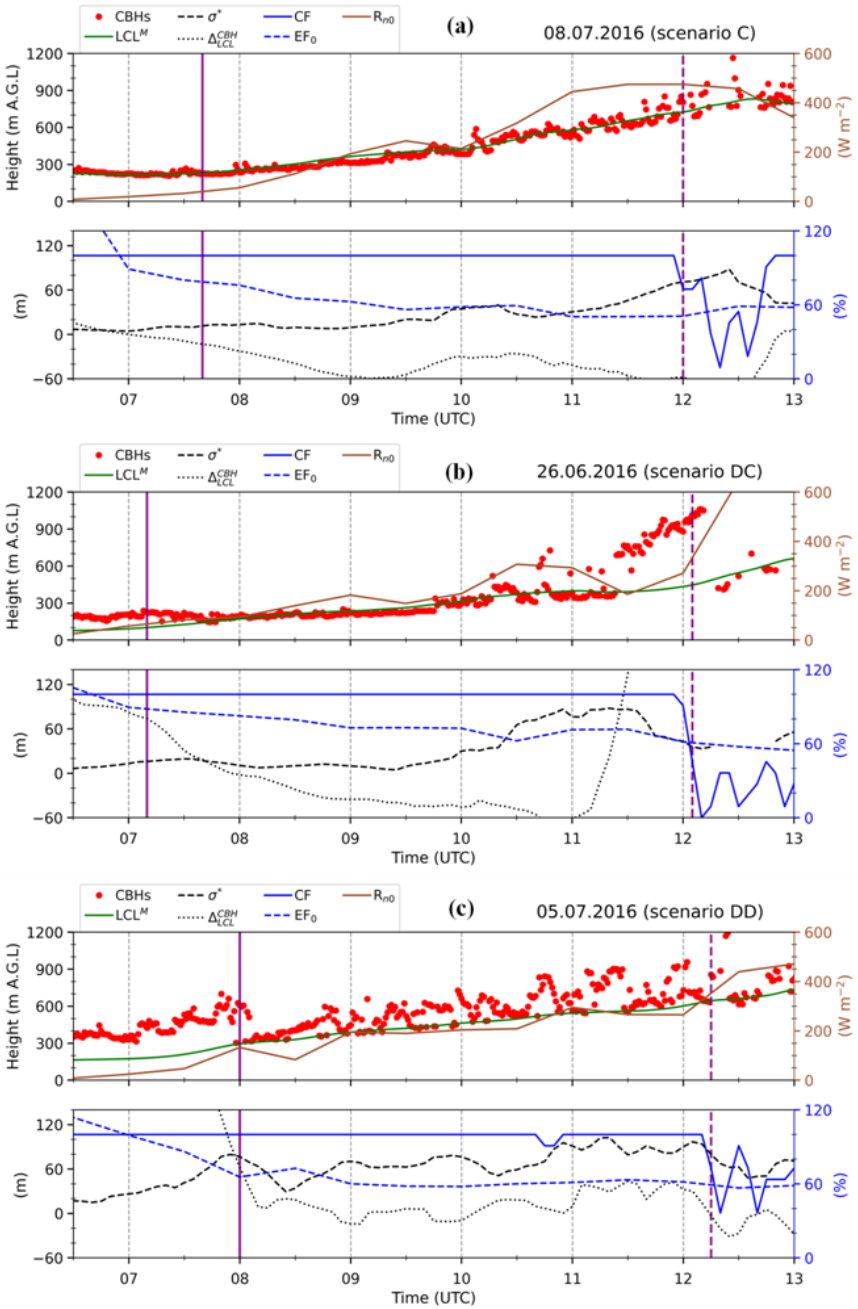

Figure 10 : Illustration of the three scenarios of LLSC evolution after the sunrise observed at Savè supersite during DACCIWA field campaign: **(a)** 08 July 2016 for scenario C, **(b)** 26 June 2016 for scenario DC and **(c)** 05 July 2016 for scenario DD. The top panels present the ceilometer-derived CBHs, the lifting condensation level (LCL) and the net radiation measured at surface (Rn_0). The bottom panels gather the cloud fraction (CF), the evaporative fraction at the surface (EF_0 in %), the standard deviation of the cloud base height in the LLSC layer (σ*) and the mean distance between cloud base height and surface-based LCL (Δ_{LCL}^{CBH}). The vertical solid and dashed lines indicate the surface-convection influence time (T_i) and the cloud deck breakup time (T_b), respectively. The Local time at Savè (Benin) is UTC +1 hour.

Whether the CBHs is close to the LCL (Fig. 10a) or not (Fig. 10b and c), it has a low variability before 07:00 UTC in these three illustrative cases, indicating a quite horizontally homogenous base of the LLSC layer before the start of the *convective phase* (as already seen in the previous section). The CBHs and the LCL in scenario C lift together after 07:30 UTC, due to thermal convective conditions in the subcloud layer. After 09:00 UTC, σ* increases gradually, but the lower bases always fit with the LCL, with Δ_{LCL}^{CBH} ranging between 0 and -40 m (Fig. 10a, lower panel). This can be interpreted as a progressive change in the LLSC base structure which is more and more heterogeneous in height but the cloud layer remains coupled with the surface all along. The evolution from stratus to stratocumulus and eventually to cumulus can hardly be established with the use of CBHs only, but CBHs already show a clear evolution from the homogeneous LLSC towards a more heterogeneous low cloud structure until the cloud deck breakup time, established when CF decreases to less than 90%, which happens at 12:00 UTC on the 08 July.

The LLSC in the scenario DC (Fig. 10b) is decoupled from the surface at the end of the *stratus phase*. The LCL starts to rise at 07:00 UTC and joins the LLSC base about 1 hour later, indicated by a decrease of the Δ_{LCL}^{CBH} down to zero (Fig. 10b, lower panel). After the coupling, the scenario DC is very similar to the scenario C and will be further commented in section 5.3.

The evolution of the LLSC in the scenario DD (Fig. 10c) is quite different compared to the two others. The LLSC layer remains decoupled from the surface until 08:00 UTC as shown by the significant departure between LCL and CBHs ($\Delta_{LCL}^{CBH} > 120\ m$, Fig. 10c, lower panel), due to a similar lifting rate of both levels. After 08:00 UTC, a new cloud layer with a base very close to the LCL ($\Delta_{LCL}^{CBH} < 40\ m$), is detected 200 m below the LLSC deck. The values of σ*, much larger than 60 m after 08:30 UTC, indicate that this new cloud layer rapidly turns to shallow cumulus clouds. Unfortunately, it is not possible to distinguish both cloud layers with the ceilometer-derived CBHs, because they remain too close to each other, with variable cloud bases and edges. But, one can suppose that the LLSC formed during the night remained above the cumulus clouds layer during part of the *convective phase*. The higher CBHs detected by the ceilometer after 09:00 UTC are the overlying LLSC base (about 200 m higher). The cumulus and LLSC layers above can however clearly be seen on the visible and infra-red full sky cameras (not shown). **In the case where the two cloud layers are superimposed, two possibilities may occur: (i) the underlying surface-convection driven cumulus cloud do not interact with the LLSC which remains decoupled from the surface, (ii) the underlying cumulus clouds develop vertically, reach the LLSC layer, and act to intermittently and locally couple it with the surface (Wood, 2012).**

Among the thirteen cases D observed at the end of the *stratus phase*, eight follow the scenario DD and five follow the scenario DC during the *convective phase* (Table A-1). The main difference between the three scenarios is that the first shallow convective clouds form when the LLSC breaks up in the scenarios C and DC, whereas in the scenario DD, shallow cumulus clouds form below the LLSC layer before it breaks up. Similar transitions were reported by previous observational and modelling studies on the stratiform low clouds (Price, 1999; Xiao et al., 2011; Ghonima et al., 2016; Mohrmann et al.,

2019; Sarkar et al., 2019; Zheng and Li, 2019; Pedruzo-Bagazgoitia et al., 2020). Especially, the transition of scenario DD is part of the conceptual model for marine stratocumulus (Xiao et al., 2011; Wood, 2012).

One can wonder what conditions lead the LLSC to either be coupled to the surface in the scenario DC, or remains possibly decoupled with the formation of an underlying cumulus layer in the scenario DD. No relevant differences in macrophysical characteristics of LLSC (base and depth) were found between the two scenarios at the end of the *stratus phase* and beginning of the *convective phase* (not shown). The LLSC with low bases are not systematically those which will be coupled to the surface at the beginning of the *convective phase*. The four parameters presented in Fig. 8, which summarise the thermodynamical conditions in the subcloud layer and above the LLSC, are not fundamentally different either between DC and DD scenarios. The relative humidity in the subcloud layer by the end of the *stratus phase* is larger than 95 % in all the cases D, and the difference between the different scenarios DD and DC is smaller than 2 % which is about the measurement accuracy. Consequently, alternative approaches are needed to identify the processes involved in the coupling of LLSC during the *convective phase*.

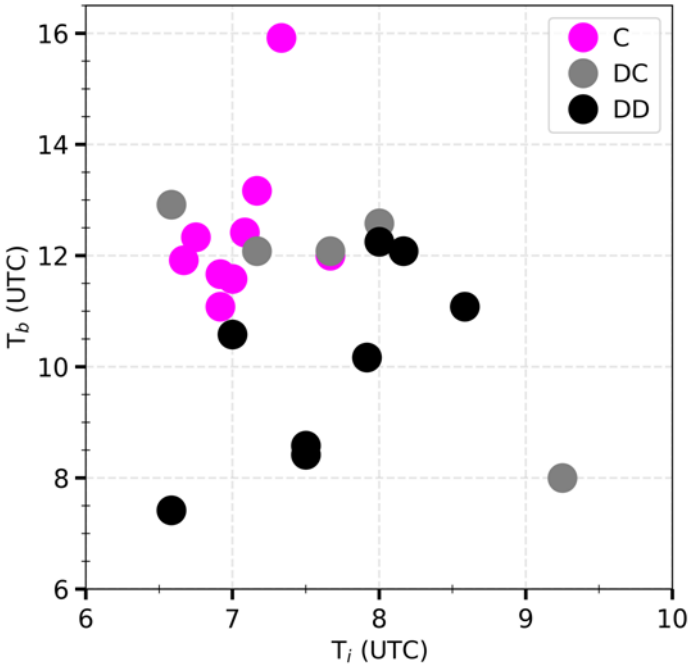

Figure 11 : LLSC breakup time (T_b) against surface-convection influence time (T_i) for the twenty-two selected cases (Table A-1). Colors stand for the three scenarios.

In conclusion, the coupling between the LLSC and the surface during the *convective phase* appears to be the key factor determining the way by which the transition towards shallow convective clouds takes place. When the LLSC is coupled to the surface (cases C and DC), it is the breakup of the cloud deck which leads to the formation of different low-level clouds type (stratocumulus or cumulus). When the LLSC is decoupled from the surface (cases DD), the convective clouds form below it. In the next paragraphs, we deeply analyze the different scenarios of the LLSC evolution.

5.2 Surface-convection and breakup times

The surface-convection influence time, T_i, indicates when the low cloud coverage is influenced by the surface-buoyancy-driven turbulence, and T_b when the low cloud breaks up. T_i is defined differently according to the scenario. For the scenario C, T_i corresponds to the time when the LLSC base starts to lift together with the LCL. After sensitivity tests, T_i is defined as the first time when LCL^M increases to at least 5 m above its value at 06:30 UTC. For the scenario DC, T_i corresponds to the time when the rising LCL reaches the LLSC base, that is when the LLSC is coupled to the surface ($\Delta_{LCL}^{CBH} < 75$ m, which is also the threshold used to differentiate C and D cases at the end of the *stratus phase* in section 4.1). For the scenario DD, T_i is the first time when new low clouds appear below the LLSC deck. As these clouds are coupled to the surface, T_i is also determined when Δ_{LCL}^{CBH} decreases to less than 75 m.

Figure 11 displays T_b and T_i for the twenty-two LLSC cases (Table A-1). T_i ranges between 06:30 and 09:15 UTC. T_b varies between 07:30 and 16:00 UTC, with breakup times occurring before 12:00 UTC for 72% of all the cases. The latter result is consistent with the findings of Dione et al. (2019) who used the infrared images from the cloud camera to define the LLSC lifetime. One can see that the LLSC breakup time is not linked to the time at which it starts to rise or at which the underlying clouds form.

For the scenario C, T_i hardly changes from one case to the other. It ranges between 06:40 and 08:00 UTC, which is not long after the sunrise (06:30 UTC). The LLSC persists at least 4.5 hours and breaks up between 11:00 and 16:00 UTC. **The latest breakup time occurring at 16:00 UTC corresponds to the 02-03 July 2016 case for which the collocated radar reveals light precipitations from higher clouds, above the LLSC layer, during the first hours of the *convective phase* (not shown), while nothing was recorded by the surface rain gauge.** This external forcing, able to enhance the liquid water content in the LLSC layer, is certainly responsible for this late breakup. Because this case is an exception and cannot easily be compared to the others, it is not considered hereafter.

For four DC cases out of five, T_i and T_b are very close to the values observed for C cases. This means that the stable stratification in the subcloud layer before the *convective phase* (which allowed the classification of this case as decoupled during the stratus phase) is rapidly eroded after sunrise and does not seem to impact the breakup time. The case for which T_b occurred at 08:00 UTC (16-17 July 2016) is removed in the following as well, because the LLSC breaks up before the LCL reaches its base.

The scenario DD presents the largest variation ranges of T_i (between 06:35 UTC and 09:00 UTC) and T_b (between 07:00 UTC and 13:00 UTC). The most striking result is that the LLSC in scenario DD often breaks up earlier than in scenarios C and DC.

Following the LES of Pedruzo-Bagazgoitia et al. (2020), the start of the *convective phase* leads to three main changes in LWP equation. First, the radiative cooling (RAD term) decreases due to the solar heating at the cloud top. Second, the ENT term also strongly decreases because the thermally-driven convection enhances the entrainment of dry and warm air from aloft in the LLSC. Third, the BASE term, which was close to zero during the *stratus phase*, comes into play during the convective phase and contributes positively to $\frac{\partial LWP}{\partial t}$. Despite the BASE term, the strong decrease of both ENT and RAD makes $\frac{\partial LWP}{\partial t}$ negative one hour after the sunrise. The RAD and ENT terms cannot be estimated during the *convective phase* with the dataset acquired at Savè because several data are missing, and, among them, the CTH.

The scenarios C and DC during the convective phase are very close to the case simulated in Pedruzo-Bagazgoitia et al. (2020) and one can expect a quite similar evolution of the terms involved in the LWP prognostic equation. Conversely, the scenario DD might be very different. The LLSC breaks up earlier, mostly before or around 10:30 UTC, when it is decoupled from the surface layer, likely due to a weaker BASE term. This hypothesis is supported by the findings of van der Dussen et al. (2014) suggesting that stratiform low clouds coupled to the surface moisture are more resistant to cloud-thinning related processes such as the entrainment of dry and warm air into the cloudy layer. The stronger variability of the breakup time for DD cases may come from the fact that the LLSC thinning depends on its interaction with the underlying cloud layer. If the latter penetrates the LLSC, local coupling can happen which induces a homogeneous layer from surface to the LLSC top, but, at the same time, the entrainment at the cloud top is enhanced by the cumulus vertical development (Wang and Lenschow, 1995).

The LLSC breakup time impacts the radiative budget at surface over the day, then the surface fluxes, and consequently, the vertical development of the ABL, as shown by Lohou et al. (2020). They estimated that the ABL height is about 900 m when the LLSC breaks up at 09:00 UTC and is 30% lower when the LLSC breaks up at 12:00 UTC. Consequently, one can expect a quite different vertical development of the ABL in C/DC cases than in DD cases.

5.3 Evolution of the LLSC horizontal structure for C and DC cases

The changes in the LLSC horizontal structure for C and DC scenarios is now further analyzed based on the evolution of the LLSC base and its standard deviation, σ^*. The cases DD are excluded from this analysis because the macrophysical characteristics of the associated LLSC cannot be determined after the underlying cloud formation. As illustrated in Fig. 10a and b, the elevation rate of the LCL, and consequently of the LLSC base, may change a lot from one case to the other. It is about 108 m h^{-1} and 67 m h^{-1} for 8 July and 26 June, respectively. One could expect that the higher this rate, the higher R_{n0},

and the more intense is the thermally-driven convection in the subcloud layer as well as the corresponding BASE term. However, no clear link is pointed out between T_b and this elevation rate of the LLSC base (not shown).

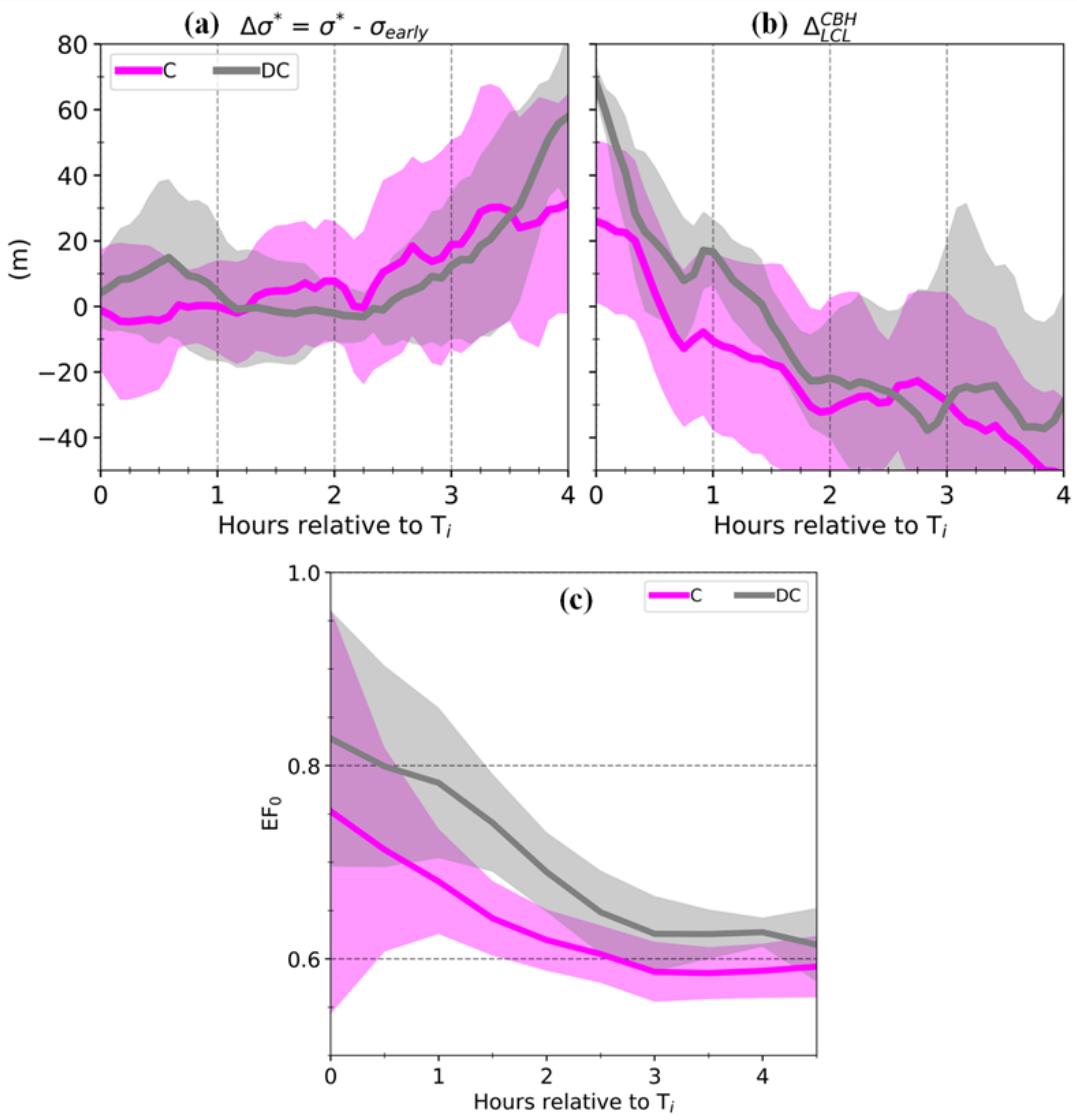

Figure 12 : Evolutions of, **(a)** Δσ*, which is the difference between the diagnostic parameter σ* and its median over the period from 04:00 to 06:30 UTC on day-D+1 (σ_{Early}), **(b)** the mean distance between the LLSC base height and surface-based LCL (Δ_{LCL}^{CBH}), **(c)** the evaporative fraction at surface (EF_0), for C (coupled) and DC (decoupled-coupled) scenarios. The solid lines indicate the median and shaded areas represent the standard deviation. The time is expressed in hours relative to surface-convection influence time (T_i).

Contrary to the LLSC base height, σ^* has a common tendency among all the C and DC cases. The evolution of σ^* with time compared to its value at T_i, σ_{Early}, is presented in Fig. 12a. A four hour-period is considered here because it is the smallest duration between T_i and T_b (Fig. 11) for the twelve C and DC cases included in this statistic. As also illustrated in Fig. 10a and Fig. 10b, σ^* remains close to σ_{Early} during at least two hours after T_i (until 09:00 UTC for 8 July and 09:30 UTC for 26 July). Consequently, during this period, the structure of the LLSC bases remains quasi-unchanged. Afterwards, σ^* progressively increases during at least 2 hours until the LLSC deck breakup. From T_i to the breakup, Δ_{LCL}^{CBH} remains lower than 70 m, with even a slight decrease in the first two hours (Fig. 12b), suggesting an enhancement of the coupling due to an increase of the thermally-driven turbulence in the subcloud layer. The combination of (1) very heterogeneous LLSC base and (2) the fact that the lowest ones remain close to the LCL during the few hours before T_b, indicates that some of the bases are coupled to the surface but some tend to be decoupled from the surface.

Eventually, the evolution of σ^* and Δ_{LCL}^{CBH} (Fig. 12) allows to define two periods between T_i and T_b: (1) the two first hours after T_i during which the LLSC is fully coupled to the surface and the homogeneity of its base is not affected yet, and, (2) the few hours before T_b during which the base of the LLSC layer becomes more and more heterogeneous and intermittently decoupled from the surface. This latter tendency can be seen in Fig. 10a upper panel after 11:00 UTC and in Fig. 10b lower panel after 10:15 UTC. A decoupling of the stratiform cloud from the surface is also observed about half an hour before the cloud deck breakup in Pedruzo-Bagazgoitia et al. (2020) simulations.

The bottom panels of Fig. 10 present the evolution of the evaporative fraction at the surface (EF_0) for the illustrative cases. Figure 12c displays the medians of this parameter over all C and DC cases. Defined as the ratio of LHF_0 to (LHF_0 + SHF_0), EF_0 larger than 0.5 means that the evapo-transpiration dominates over the warming. This is in average the case at Savè during the DACCIWA campaign (Kalthoff et al., 2018). Figure 12c shows that the median of EF_0 decreases from around 0.75 at T_i to 0.6 at the LLSC breakup. The predominance of the evapo-transpiration over the sensible heat flux, particularly during the two first hours after T_i, and the full coupling of the LLSC to the surface, might contribute to maintain the LLSC through the BASE term. The LLSC base is indeed strongly homogeneous. The decrease of EF_0 and its levelling at 0.6 implies a faster increase of SHF_0 than LHF_0. One can then expect a larger contribution of $\overline{w'\theta_l'}^b$ and a smaller one from $\overline{w'q_t'}^b$ in BASE term with time. **This favours the convection in the LLSC which enhances the entrainment, at the expense of the cloud moistening by the underlying turbulent mixing.** In addition to this, the final intermittent decoupling of the LLSC from the surface likely contribute, together with the decrease of RAD and ENT terms (Pedruzo-Bagazgoitia et al., 2020), to the LLSC breakup.

It appears that, the LLSC and the timing of its evolution in the scenarios C and DC are very similar during the *convective phase*. In these scenarios, the LLSC keeps the same characteristics in terms of coupling and base homogeneity during two hours after T_i. Afterwards and until its breakup, the LLSC becomes more and more heterogeneous and intermittently decoupled from the surface. These two steps are in phase with the evolution of the EF_0 which likely impacts the BASE term that is the only positive contribution to LWP budget during the *convective phase*.

6 Summary and conclusion

The breakup of the almost daily LLSC during monsoon season in southern West Africa is the object of this study. It is based on the analysis of a set of twenty-two precipitation-free LLSC occurrences observed during the DACCIWA field experiment at Savè supersite. The diurnal cycle of the LLSC consists of four main stages and this study addresses the two latest, the *stratus* and *convective* phases. We used the ground-based observational data collected by (i) ceilometer and cloud radar for macrophysical properties of the cloud layer, (ii) energy balance and weather stations for the atmospheric conditions near the surface, and finally, (iii) radiosoundings and UHF wind profiler for the thermodynamical and dynamical conditions within the low-troposphere. From these measurements, some diagnostics of the LLSC layer are estimated, including: the cloud-base height, the cloud coverage fraction, the cloud base homogeneity and the cloud coupling with the surface. The coupling was assessed by the distance between the LLSC base height and the lifting condensation level: the cloud layer is coupled to the surface when these two levels coincide. Our main results are summarized in Fig. 13 by a schematic illustration.

At the beginning of the *stratus phase* (after 22:00 UTC), the LLSC is decoupled from the surface in all the studied cases, except in one. Within the following four hours, in nine among the twenty-two cases, the LLSC base lowers in such way that the cloud layer gets coupled to the surface (referenced as cases C, Fig. 13c). In the thirteen other cases (referenced as cases D, Fig. 13a and b), the LLSC remains decoupled from the surface. The weak thermodynamical differences observed between C and D cases at Savè can hardly explain the coupling which occurs in C cases. However, the cases C occurred preferentially between 27 June and 8 July 2016, a period with a well-established monsoon flow over West-Africa, especially over DACCIWA investigated area. Most of the cases D are observed during the monsoon onset period or during disturbed sub-periods after 08 July 2016. If the synoptic conditions of the monsoon flow play a role on the LLSC coupling with the surface, it could be through the thermodynamical conditions, which were hardly highlighted with Savè data set. It could also be through large scale dynamical parameters like large scale subsidence, which is an important factor to LWP budget and could not be determined precisely for every day with Savè data set. The analyses of the stable and jet phase by Adler et al. (2019) and Babić et al. (2019a,b) outline a complex imbrications of different processes in LLSC formation. Similarly, we conclude that the LLSC coupling to the surface during the *stratus phase* is also based on different processes for which a slight intensity change may have an important impact.

The Savè data set allowed us to estimate the most important terms of the LWP tendency equation at the end of the *stratus phase*, notably the radiative, entrainment and subsidence terms. Our values are very close to those found by Pedruzo-Bagazgoitia et al. (2020) in a numerical study of a DACCIWA case. Since the LLSC layer develops in the monsoon flow, it is warmer and characterised by weaker temperature and humidity jumps at its top, but with same magnitude order of cloud-top radiative cooling, compared to marine stratocumulus over subtropical region.

During the *convective phase* of the LLSC diurnal cycle, a new separation occurs among the D cases. In some of them, the LLSC couples to the surface while the lifting condensation level rises with the thermally-driven convection at the surface

(Fig. 13b). Therefore, the LLSC deck may follow three scenarios until its breakup: (1) the scenario DD for "decoupled-decoupled" (followed by most of D cases, Fig. 13a), (2) the scenario DC for "decoupled-coupled" (followed the other D cases, Fig. 13b), and (3) the scenario C (followed by all the C cases of the *stratus phase*, Fig. 13c). The scenarios C and DD are the most frequent among the twenty-two studied cases with nine and eight occurrences respectively. The reason why the cases D follow DC or DD was not clearly identified.

Typically, the scenarios C and DC are quite similar and consist of two steps: (ii) the first two hours during which the LLSC layer lifts but remains fully coupled to the surface and the homogeneity of its base is not affected yet, (ii) the few hours preceding the breakup time during which the cloud layer is sometime decoupled from the surface as its base becomes more and more heterogeneous. In these two scenarios, the breakup of the LLSC deck leads to a transition towards shallow cumulus clouds. This occurs at around 11:00 UTC or later, approximately more than 4.5 hours after the LLSC starts to lift. In the scenario DD, cumulus clouds, triggered by convectively mixed layer, form below the LLSC deck before its breakup. The breakup time in this scenario varies strongly between 07:30 UTC and noon. But in most of the cases, it occurs before 11:00 UTC. The earlier breakup occurring in the scenario DD outlines the importance of the coupling with surface for the LLSC maintenance after the sunrise. Thus, we conclude that, in SWA conditions, the coupling between the LLSC and the surface is a key factor for its evolution during daylight hours. **It determines the LLSC lifetime and the way by which the transition towards shallow convective clouds occurs. The coupled LLSC last longer (breakup time at 12:00 UTC in average) than decoupled cases (breakup time at 10:00 UTC in average). According to Lohou et al. (2020), such a difference in breakup time leads to a reduction of about 15% of net radiation at surface and of ABL vertical development during the day for coupled cases compared to decoupled one.**

From these results, it appears important to correctly simulate the coupling of the nocturnal LLSC layer for a better representation of West African monsoon features in global climate and weather model simulations. However, the processes responsible for the coupling at different stages of the LLSC diurnal cycle (during the *stratus phase* for C cases (Fig. 13c) and during the *convective phase* for DC scenario (Fig. 13b)) are not easy to identify. The coupling rather results from a combination of several processes than a well distinct and predominant one. Thus, it seems very difficult to advise one improvement in the model. **The aerosol loading in the low-troposphere is a potential factor controlling the LLSC evolution and lifetime (Deetz et al., 2018; Mohrmann et al., 2019). The airborne measurements of low-cloud properties over SWA during DACCIWA (Flamant et al., 2017) could be used to assess the microphysical role for aerosol in the LLSC evolution scenario. This may help to differentiate the scenarios DC and DD.** Furthermore, the potentially large influence of middle-level clouds on the LLSC remains also an opened question and was not objectively addressed in this study. It would be also interesting to study how the LLSC breakup over SWA might change in future climate.

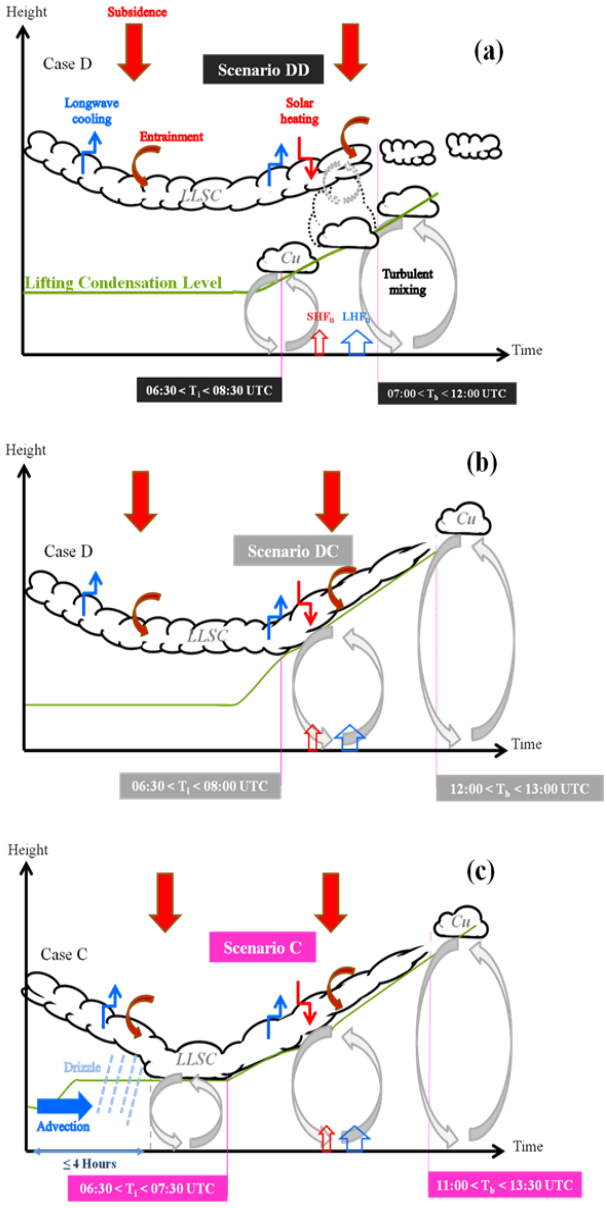

Figure 13 : Schematic illustration of the main findings of the present study. It portrays the typical evolutions of the LLSC sampled at Savè (Benin where local time equals UTC +1 hour), during DACCIWA field experiment. The different scenarios and their characteristic times as well as the relevant physical processes are illustrated (the different arrows signification is indicated in **a,** and remains the same in **b** and **c**). The representation encompasses the stratus and convective phases of the LLSC diurnal cycle. The width of the arrows representing the near-surface latent and sensible heat fluxes (LHF_0 and SHF_0 resp.) correspond to their relative proportions. Typically, the LLSC forms decoupled from the surface (**a**, **b** and **c**). For the D cases (**a** and **b**), the LLSC remains uncoupled all along the stratus phase. For the C cases (**c**), the LLSC gets coupled to surface within the four hours after its formation as the cloud base descents significantly and the LCL increases potentially because of drier and cooler air horizontal advection (horizontal blue filled arrow in **c**), and drizzle formation in the subcloud layer (**c**). In all the C cases, the LLSC evolves by the scenario C, in which the cloud layer lifts with the growing convective boundary layer, the subsequent cloud deck breakup leads to shallow convective clouds formation. In the scenario DD (**a**), followed by most of the D cases, surface-convection driven cumulus forms below the LLSC deck before its breakup. The others cases D evolve by the scenario DC (**b**), in which the LLSC couples with the surface as the convective boundary layer top joins the LLSC base, and the subsequent LLSC evolution is similar to the scenario C.

Data availability. The data used in this study are available in the BAOBAB (Base Afrique de l'Ouest Beyond AMMA Base) database (https://baobab.sedoo.fr/DACCIWA/).

Author contributions. FL, NK, ML, CD, BA and XPB performed the measurements at Savè supersite. MZ processed the data and carried out the analysis with contributions from FL and ML. MZ wrote the paper with contributions from all co-authors.

Competing interests. The authors declare that they have no conflict of interest.

Acknowledgements. The DACCIWA project has received funding from the European Union Seventh Framework Programme (FP7/2007-2013) under grant agreement no. 603502. The first author thanks Laboratoire d'Aérologie, Université de Toulouse, France for hosting the research activities. We would also like to thank two anonymous reviewers for their helpful comments and suggestions.

Financial support. This study received the financial support of the PASMU (Pollution de l'Air et Santé dans les Milieux Urbains de Côte d'Ivoire) project funded by the programme of Debt Reduction-Development Contracts (C2Ds) managed by the Institute of Research and Development (IRD, France).

Synoptic conditions	**Onset**		**Post-Onset**																	**Recovery**		
Months	**June 2016**						**July 2016**															
Day-D+1	20	22	26	27	29	30	01	02	03	04	05	06	07	08	10	11	17	18	19	27	28	29
N° IOP	--	--	03	--	04	--	05	--	06	--	07	--	--	08	--	09	--	11	--	14	--	--
LLSC at the end of the stratus phase (section 4)																						
CBH	206	370	204	226	249	174	53	70	91	100	277	147	292	253	299	380	306	338	136	260	206	208
Depth	813	499	185	404	381	306	607	320	--	470	502	452	337	407	--	--	384	412	313	385	573	--
$Shear^{+}$	6.7	2.2	0.1	6.0	0.8	0.4	0.5	4.5	--	43.3	5.5	12.3	17.2	7.1	--	--	--	--	2.6	--	--	--
$\theta^{-} - 290$	7.2	7.5	6.7	7.5	7.3	7.2	6.9	6.6	--	6.3	7.7	7.2	8.1	7.8	--	--	--	--	6.3	--	--	--
$\Delta\theta_l$	3.5	2.6	1.4	2.2	2.3	1.7	3.7	1.9	--	4.7	4.2	2.7	1.9	2.8	--	--	--	--	2.4	--	--	--
q^{-}	16.7	15.7	15.9	16.8	16.4	16.8	17.0	16.8	--	16.8	16.3	17.0	16.7	16.8	--	--	--	--	16.2	--	--	--
Δq_t	-3.0	-2.1	-0.1	-1.4	-1.3	-1.5	-1.3	-0.6	--	-0.1	-1.5	-1.0	-1.3	-0.7	--	--	--	--	-0.2	--	--	--
RAD	65.9	62.7	45.2	53.3	52.4	49.7	56.0	53.4	--	59.2	60.8	56.5	57.5	54.9	--	--	--	--	56.5	--	--	--
ENT	-.02	-9.7	-0.2	-3.9	-6.1	-10.3	-0.5	1.2	--	-6.4	-11.6	-0.4	-7.0	-2.1	--	--	--	--	-1.0	--	--	--
SUBS	-60.9	-47.9	-23.8	-38.8	-34.4	-35.5	-36.5	-35.7	--	-23.5	-28.9	-37.6	-40.5	-31.6	--	--	--	--	-29.3	--	--	--
LLSC during the convective phase (section 5)																						
Scenarios	DD	DD	DC	C	DD	C	C	C	C	C	DD	C	DC	C	DD	DD	DC	DD	C	DC	DD	DC
T_i	0835	0730	0715	0700	0810	0705	0710	0655	0720	0655	0805	0640	0635	0740	0705	0755	0910	0730	0645	0745	0635	0805
T_b	1105	0835	1205	1135	1205	1225	1310	1140	1555	1105	1215	1155	1255	1200	1035	1010	0800	0825	1220	1205	0725	1235

Table A-1 : Summary of the LLSC features at the end of the stratus phase (section 4) and during the convective phase (section 5) for the twenty-two occurrences at Savè supersite analyzed in this study. The Day-D+1 of the night-to-day transition and the eventual corresponding IOP number are indicated. The main synoptic conditions defined by Knippertz et al. (2017) in which they fall are mentioned at the top. The Cloud base height (CBH in m a.g.l) and depth (m) are estimated from the ceilometer and cloud radar measurements. The contribution of wind shear in turbulence production at the cloud top ($Shear^{+}$, in 10^{-5} s^{-2}), the thermodynamical properties of the cloud, $\theta^{-}$and $\Delta\theta_l$ in K, q^{-}, Δq_t and g kg^{-1} as well as the LWP budget terms radiative (RAD), entrainment (ENT) and subsidence (SUBS), in g m^{-2} h^{-1}, are derived from 05:00 UTC standard radiosoundings. They are estimated only for the fourteen cases for which the radiosonde flew into the LLSC layer. The scenario of evolution after the sunrise and its characteristic times, the surface-convection influence (T_i) and breakup (T_b) times are indicated in the format HHMM UTC. C, DC and DD stand for “coupled”, “decoupled-coupled” and “decoupled-decoupled” scenarios respectively. The local time at Savè in (Benin) is UTC + 1 hour.

References

Adler, B., Kalthoff, N. and Gantner, L.: Nocturnal low-level clouds over southern West Africa analysed using high-resolution simulations, Atmospheric Chemistry and Physics, 17(2), 899–910, doi:10.5194/acp-17-899-2017, 2017.

Adler, B., Babić, K., Kalthoff, N., Lohou, F., Lothon, M., Dione, C., Pedruzo-Bagazgoitia, X. and Andersen, H.: Nocturnal low-level clouds in the atmospheric boundary layer over southern West Africa: an observation-based analysis of conditions and processes, Atmospheric Chemistry and Physics, 19(1), 663–681, doi:10.5194/acp-19-663-2019, 2019.

Babić, K., Adler, B., Kalthoff, N., Andersen, H., Dione, C., Lohou, F., Lothon, M. and Pedruzo-Bagazgoitia, X.: The observed diurnal cycle of low-level stratus clouds over southern West Africa: a case study, Atmospheric Chemistry and Physics, 19(2), 1281–1299, doi:10.5194/acp-19-1281-2019, 2019a.

Babić, K., Kalthoff, N., Adler, B., Quinting, J. F., Lohou, F., Dione, C. and Lothon, M.: What controls the formation of nocturnal low-level stratus clouds over southern West Africa during the monsoon season?, Atmos. Chem. Phys., 19(21), 13489–13506, doi:10.5194/acp-19-13489-2019, 2019b.

Bretherton, C. S., Krueger, S. K., Wyant, M. C., Bechtold, P., Van Meijgaard, E., Stevens, B. and Teixeira, J.: A GCSS Boundary-Layer Cloud Model Intercomparison Study Of The First Astex Lagrangian Experiment, Boundary-Layer Meteorology, 93(3), 341–380, doi:10.1023/A:1002005429969, 1999.

Christensen, M. W., Carrió, G. G., Stephens, G. L. and Cotton, W. R.: Radiative Impacts of Free-Tropospheric Clouds on the Properties of Marine Stratocumulus, Journal of the Atmospheric Sciences, 70(10), 3102–3118, doi:10.1175/JAS-D-12-0287.1, 2013.

Dearden, C., Hill, A., Coe, H. and Choularton, T.: The role of droplet sedimentation in the evolution of low-level clouds over southern West Africa, Atmos. Chem. Phys., 18(19), 14253–14269, doi:10.5194/acp-18-14253-2018, 2018.

Deetz, K., Vogel, H., Knippertz, P., Adler, B., Taylor, J., Coe, H., Bower, K., Haslett, S., Flynn, M., Dorsey, J., Crawford, I., Kottmeier, C. and Vogel, B.: Cloud and aerosol radiative effects as key players for anthropogenicchanges in atmospheric dynamics over southernWest Africa, Atmos. Chem. Phys. Discuss., 1–36, doi:10.5194/acp-2018-186, 2018.

Dione, C., Lohou, F., Lothon, M., Adler, B., Babić, K., Kalthoff, N., Pedruzo-Bagazgoitia, X., Bezombes, Y. and Gabella, O.: Low-level stratiform clouds and dynamical features observed within the southern West African monsoon, Atmos. Chem. Phys., 19(13), 8979–8997, doi:10.5194/acp-19-8979-2019, 2019.

van der Dussen, J. J., de Roode, S. R. and Siebesma, A. P.: Factors Controlling Rapid Stratocumulus Cloud Thinning, J. Atmos. Sci., 71(2), 655–664, doi:10.1175/JAS-D-13-0114.1, 2014.

van der Dussen, J. J., de Roode, S. R. and Siebesma, A. P.: How large-scale subsidence affects stratocumulus transitions, Atmos. Chem. Phys., 16(2), 691–701, doi:10.5194/acp-16-691-2016, 2016.

Duynkerke, P. G., de Roode, S. R., van Zanten, M. C., Calvo, J., Cuxart, J., Cheinet, S., Chlond, A., Grenier, H., Jonker, P. J., Köhler, M., Lenderink, G., Lewellen, D., Lappen, C.-L., Lock, A. P., Moeng, C.-H., Müller, F., Olmeda, D., Piriou, J.-M., Sánchez, E. and Sednev, I.: Observations and numerical simulations of the diurnal cycle of the EUROCS stratocumulus case, Q. J. R. Meteorol. Soc., 130(604), 3269–3296, doi:10.1256/qj.03.139, 2004.

Emetere, M. E.: Investigations on aerosols transport over micro- and macro-scale settings of West Africa, Environmental Engineering Research, 22(1), 75–86, doi:10.4491/eer.2016.080, 2016.

Faloona, I., Lenschow, D. H., Campos, T., Stevens, B., van Zanten, M., Blomquist, B., Thornton, D., Bandy, A. and Gerber, H.: Observations of Entrainment in Eastern Pacific Marine Stratocumulus Using Three Conserved Scalars, J. Atmos. Sci., 62(9), 3268–3285, doi:10.1175/JAS3541.1, 2005.

Fitzpatrick, R. G. J., Bain, C. L., Knippertz, P., Marsham, J. H. and Parker, D. J.: The West African Monsoon Onset: A Concise Comparison of Definitions, Journal of Climate, 28(22), 8673–8694, doi:10.1175/JCLI-D-15-0265.1, 2015.

Flamant, C., Knippertz, P., Fink, A. H., Akpo, A., Brooks, B., Chiu, C. J., Coe, H., Danuor, S., Evans, M., Jegede, O., Kalthoff, N., Konaré, A., Liousse, C., Lohou, F., Mari, C., Schlager, H., Schwarzenboeck, A., Adler, B., Amekudzi, L., Aryee, J., Ayoola, M., Batenburg, A. M., Bessardon, G., Borrmann, S., Brito, J., Bower, K., Burnet, F., Catoire, V., Colomb, A., Denjean, C., Fosu-Amankwah, K., Hill, P. G., Lee, J., Lothon, M., Maranan, M., Marsham, J., Meynadier, R., Ngamini, J.-B., Rosenberg, P., Sauer, D., Smith, V., Stratmann, G., Taylor, J. W., Voigt, C. and Yoboué, V.: The Dynamics-Aerosol-Chemistry-Cloud Interactions in West Africa field campaign: Overview and research highlights, Bull. Amer. Meteor. Soc., doi:10.1175/BAMS-D-16-0256.1, 2017.

Garratt, J. R.: The Atmospheric Boundary Layer, Cambridge University Press., 1994.

Ghonima, M. S., Heus, T., Norris, J. R. and Kleissl, J.: Factors Controlling Stratocumulus Cloud Lifetime over Coastal Land, J. Atmos. Sci., 73(8), 2961–2983, doi:10.1175/JAS-D-15-0228.1, 2016.

Handwerker, J., Scheer, S. and Gamer, T.: DACCIWA field campaign, Savè super-site, Cloud and precipitation, , doi:10.6096/dacciwa.1686, 2016.

Hannak, L., Knippertz, P., Fink, A. H., Kniffka, A. and Pante, G.: Why Do Global Climate Models Struggle to Represent Low-Level Clouds in the West African Summer Monsoon?, J. Climate, 30(5), 1665–1687, doi:10.1175/JCLI-D-16-0451.1, 2017.

Kalthoff, N., Lohou, F., Brooks, B., Jegede, G., Adler, B., Babić, K., Dione, C., Ajao, A., Amekudzi, L. K., Aryee, J. N. A., Ayoola, M., Bessardon, G., Danuor, S. K., Handwerker, J., Kohler, M., Lothon, M., Pedruzo-Bagazgoitia, X., Smith, V., Sunmonu, L., Wieser, A., Fink, A. H. and Knippertz, P.: An overview of the diurnal cycle of the atmospheric boundary layer during the West African monsoon season: results from the 2016 observational campaign, Atmospheric Chemistry and Physics, 18(4), 2913–2928, doi:10.5194/acp-18-2913-2018, 2018.

Knippertz, P., Fink, A. H., Schuster, R., Trentmann, J., Schrage, J. M. and Yorke, C.: Ultra-low clouds over the southern West African monsoon region, Geophysical Research Letters, 38(21), doi:10.1029/2011GL049278, 2011.

Knippertz, P., Coe, H., Chiu, J. C., Evans, M. J., Fink, A. H., Kalthoff, N., Liousse, C., Mari, C., Allan, R. P., Brooks, B., Danour, S., Flamant, C., Jegede, O. O., Lohou, F. and Marsham, J. H.: The DACCIWA Project: Dynamics–Aerosol–Chemistry–Cloud Interactions in West Africa, Bulletin of the American Meteorological Society, 96(9), 1451–1460, doi:10.1175/BAMS-D-14-00108.1, 2015.

Knippertz, P., Fink, A. H., Deroubaix, A., Morris, E., Tocquer, F., Evans, M. J., Flamant, C., Gaetani, M., Lavaysse, C., Mari, C., Marsham, J. H., Meynadier, R., Affo-Dogo, A., Bahaga, T., Brosse, F., Deetz, K., Guebsi, R., Latifou, I., Maranan, M., Rosenberg, P. D. and Schlueter, A.: A meteorological and chemical overview of the DACCIWA field campaign in West Africa in June–July 2016, Atmospheric Chemistry and Physics, 17(17), 10893–10918, doi:10.5194/acp-17-10893-2017, 2017.

Kohler, M., Kalthoff, N., Seringer, J. and Kraut, S.: DACCIWA field campaign, Savè super-site, Surface measurements, , doi:10.6096/dacciwa.1690, 2016.

Lilly, D. K.: Models of cloud-topped mixed layers under a strong inversion, Q.J.R. Meteorol. Soc., 94(401), 292–309, doi:10.1002/qj.49709440106, 1968.

van der Linden, R., Fink, A. H. and Redl, R.: Satellite-based climatology of low-level continental clouds in southern West Africa during the summer monsoon season: Low-level clouds in southern West Africa, Journal of Geophysical Research: Atmospheres, 120(3), 1186–1201, doi:10.1002/2014JD022614, 2015.

Lohou, F., Kalthoff, N., Adler, B., Babić, K., Dione, C., Lothon, M., Pedruzo-Bagazgoitia, X. and Zouzoua, M.: Conceptual model of diurnal cycle of low-level stratiform clouds over southern West Africa, Atmospheric Chemistry and Physics, 20(4), 2263–2275, doi:https://doi.org/10.5194/acp-20-2263-2020, 2020.

Lothon, M., Saïd, F., Lohou, F. and Campistron, B.: Observation of the Diurnal Cycle in the Low Troposphere of West Africa, Mon. Wea. Rev., 136(9), 3477–3500, doi:10.1175/2008MWR2427.1, 2008.

Mauder, M., Cuntz, M., Drüe, C., Graf, A., Rebmann, C., Schmid, H. P., Schmidt, M. and Steinbrecher, R.: A strategy for quality and uncertainty assessment of long-term eddy-covariance measurements, Agricultural and Forest Meteorology, 169, 122–135, doi:10.1016/j.agrformet.2012.09.006, 2013.

Mechem, D. B., Kogan, Y. L. and Schultz, D. M.: Large-Eddy Simulation of Post-Cold-Frontal Continental Stratocumulus, J. Atmos. Sci., 67(12), 3835–3853, doi:10.1175/2010JAS3467.1, 2010.

Mohrmann, J., Bretherton, C. S., McCoy, I. L., McGibbon, J., Wood, R., Ghate, V., Albrecht, B., Sarkar, M., Zuidema, P. and Palikonda, R.: Lagrangian Evolution of the Northeast Pacific Marine Boundary Layer Structure and Cloud during CSET, Monthly Weather Review, 147(12), 4681–4700, doi:10.1175/MWR-D-19-0053.1, 2019.

Parker, D. J., Burton, R. R., Diongue-Niang, A., Ellis, R. J., Felton, M., Taylor, C. M., Thorncroft, C. D., Bessemoulin, P. and Tompkins, A. M.: The diurnal cycle of the West African monsoon circulation, Quarterly Journal of the Royal Meteorological Society, 131(611), 2839–2860, doi:10.1256/qj.04.52, 2005.

Pedruzo-Bagazgoitia, X., de Roode, S. R., Adler, B., Babić, K., Dione, C., Kalthoff, N., Lohou, F., Lothon, M. and Vilà-Guerau de Arellano, J.: The diurnal stratocumulus-to-cumulus transition over land in southern West Africa, Atmos. Chem. Phys., 20(5), 2735–2754, doi:10.5194/acp-20-2735-2020, 2020.

Price, J. D.: Observations of stratocumulus cloud break-up over land, Q.J Royal Met. Soc., 125(554), 441–468, doi:10.1002/qj.49712555404, 1999.

Ricchiazzi, P., Yang, S., Gautier, C. and Sowle, D.: SBDART: A Research and Teaching Software Tool for Plane-Parallel Radiative Transfer in the Earth's Atmosphere, Bull. Amer. Meteor. Soc., 79(10), 2101–2114, doi:10.1175/1520-0477(1998)079<2101:SARATS>2.0.CO;2, 1998.

Romps, D. M.: Exact Expression for the Lifting Condensation Level, Journal of the Atmospheric Sciences, 74(12), 3891–3900, doi:10.1175/JAS-D-17-0102.1, 2017.

de Roode, S. R., Sandu, I., van der Dussen, J. J., Ackerman, A. S., Blossey, P., Jarecka, D., Lock, A., Siebesma, A. P. and Stevens, B.: Large-Eddy Simulations of EUCLIPSE–GASS Lagrangian Stratocumulus-to-Cumulus Transitions: Mean State, Turbulence, and Decoupling, J. Atmos. Sci., 73(6), 2485–2508, doi:10.1175/JAS-D-15-0215.1, 2016.

S. Derrien, Y. Bezombes, G. Bret, O. Gabella, C. Jarnot, P. Medina, E. Piques, C. Delon, C. Dione, B. Campistron, P. Durand, C. Jambert, F. Lohou, M. Lothon, F. Pacifico and Y. Meyerfeld: DACCIWA field campaign, Savè super-site, UPS instrumentation, 2016.

Sandu, I. and Stevens, B.: On the Factors Modulating the Stratocumulus to Cumulus Transitions, J. Atmos. Sci., 68(9), 1865–1881, doi:10.1175/2011JAS3614.1, 2011.

Sarkar, M., Zuidema, P., Albrecht, B., Ghate, V., Jensen, J., Mohrmann, J. and Wood, R.: Observations Pertaining to Precipitation within the Northeast Pacific Stratocumulus-to-Cumulus Transition, Monthly Weather Review, 148(3), 1251–1273, doi:10.1175/MWR-D-19-0235.1, 2019.

Schrage, J. M. and Fink, A. H.: Nocturnal Continental Low-Level Stratus over Tropical West Africa: Observations and Possible Mechanisms Controlling Its Onset, Monthly Weather Review, 140(6), 1794–1809, doi:10.1175/MWR-D-11-00172.1, 2012.

Schuster, R., Fink, A. H. and Knippertz, P.: Formation and Maintenance of Nocturnal Low-Level Stratus over the Southern West African Monsoon Region during AMMA 2006, Journal of the Atmospheric Sciences, 70(8), 2337–2355, doi:10.1175/JAS-D-12-0241.1, 2013.

Siems, S. T., Lenschow, D. H. and Bretherton, C. S.: A Numerical Study of the Interaction between Stratocumulus and the Air Overlying It, J. Atmos. Sci., 50(21), 3663–3676, doi:10.1175/1520-0469(1993)050<3663:ANSOTI>2.0.CO;2, 1993.

Stevens, B.: Bulk boundary-layer concepts for simplified models of tropical dynamics, Theor. Comput. Fluid Dyn., 20(5–6), 279–304, doi:10.1007/s00162-006-0032-z, 2006.

Stevens, B., Moeng, C.-H., Ackerman, A. S., Bretherton, C. S., Chlond, A., de Roode, S., Edwards, J., Golaz, J.-C., Jiang, H., Khairoutdinov, M., Kirkpatrick, M. P., Lewellen, D. C., Lock, A., Müller, F., Stevens, D. E., Whelan, E. and Zhu, P.: Evaluation of Large-Eddy Simulations via Observations of Nocturnal Marine Stratocumulus, Mon. Wea. Rev., 133(6), 1443–1462, doi:10.1175/MWR2930.1, 2005.

Stull, R. B., Ed.: An Introduction to Boundary Layer Meteorology, Springer Netherlands, Dordrecht. [online] Available from: http://link.springer.com/10.1007/978-94-009-3027-8 (Accessed 10 October 2016), 1988.

vanZanten, M. C., Duynkerke, P. G. and Cuijpers, J. W. M.: Entrainment Parameterization in Convective Boundary Layers, J. Atmos. Sci., 56(6), 813–828, doi:10.1175/1520-0469(1999)056<0813:EPICBL>2.0.CO;2, 1999.

Wang, Q. and Lenschow, D.: An Observational Study of the Role of Penetrating Cumulus in a Marine Stratocumulus-Topped Boundary Layer, Journal of The Atmospheric Sciences - J ATMOS SCI, 52, 2778–2787, doi:10.1175/1520-0469(1995)052<2778:AOSOTR>2.0.CO;2, 1995.

Wieser, A., Adler, B. and Deny, B.: DACCIWA field campaign, Savè super-site, Thermodynamic data sets, , doi:10.6096/dacciwa.1659, 2016.

Wood, R.: Stratocumulus Clouds, Mon. Wea. Rev., 140(8), 2373–2423, doi:10.1175/MWR-D-11-00121.1, 2012.

Xiao, H., Wu, C.-M. and Mechoso, C. R.: Buoyancy reversal, decoupling and the transition from stratocumulus to shallow cumulus topped marine boundary layers, Clim Dyn, 37(5–6), 971–984, doi:10.1007/s00382-010-0882-3, 2011.

Zheng, Y. and Li, Z.: Episodes of Warm-Air Advection Causing Cloud-Surface Decoupling During the MARCUS, J. Geophys. Res. Atmos., 124(22), 12227–12243, doi:10.1029/2019JD030835, 2019.

Zheng, Y., Rosenfeld, D., Zhu, Y. and Li, Z.: Satellite-Based Estimation of Cloud Top Radiative Cooling Rate for Marine Stratocumulus, Geophys. Res. Lett., 46(8), 4485–4494, doi:10.1029/2019GL082094, 2019.

Zhu, P., Albrecht, B. and Gottschalck, J.: Formation and Development of Nocturnal Boundary Layer Clouds over the Southern Great Plains, Journal of the Atmospheric Sciences, 58, doi:10.1175/1520-0469(2001)058<1409:FADONB>2.0.CO;2, 2001.